Measuring cell viscoelastic properties using a microfluidic extensional flow device

L Guillou[†], JB Dahl[†], JG Lin[†], AI Barakat, J Husson, SJ Muller, S Kumar[*]

†These authors contributed equally to this work
*Corresponding author

RUNNING TITLE
Microfluidics for cell mechanics

ABSTRACT

The quantification of cellular mechanical properties is of tremendous interest in biology and medicine. Recent microfluidic technologies that infer cellular mechanical properties based on analysis of cellular deformations during microchannel traversal have dramatically improved throughput over traditional single-cell rheological tools, yet the extraction of material parameters from these measurements remains quite complex due to challenges such as confinement by channel walls and the domination of complex inertial forces. Here we describe a simple microfluidic platform that uses hydrodynamic forces at low Reynolds number and low confinement to elongate single cells near the stagnation point of a planar extensional flow. In tandem, we present a novel analytical framework that enables determination of cellular viscoelastic properties (stiffness and fluidity) from these measurements. We validated our system and analysis by measuring the stiffness of cross-linked dextran microparticles, which yielded reasonable agreement with previously reported values and our micropipette aspiration measurements. We then measured viscoelastic properties of 3T3 fibroblasts and glioblastoma tumor initiating cells (GBM TICs). Our system captures the expected changes in elastic modulus induced in 3T3s and TICs in response to agents that soften (cytochalasin D) or stiffen (paraformaldehyde) the cytoskeleton. The simplicity of the device coupled with our analytical model allows straightforward measurement of the viscoelastic properties of cells and soft, spherical objects.

INTRODUCTION

While it has been long understood that soluble factors from the cellular microenvironment can strongly influence cellular behavior, it is becoming increasingly clear that physical and especially mechanical inputs can also affect cell behaviors such as migration, proliferation and differentiation (1-4). Cells frequently respond to mechanical stimuli by adaptively tuning their intrinsic mechanical properties, and significant evidence suggests that this "mechanoadaptation" is key to transducing these inputs into biochemical signals that mediate cell behavior. Moreover, because disease states are often accompanied by changes in cell and tissue mechanics, there has been growing interest in using cell mechanical properties as a label-free biomarker (5-9). As a result, there is much interest in developing platforms to quickly and accurately quantify cellular mechanical properties. These new platforms would not only facilitate advances in understanding how cells stabilize their shape and process mechanical cues but also give rise to novel clinical diagnostic tools.

Traditional techniques to study the mechanical properties of single cells include micropipette aspiration (MPA), atomic force microscopy (AFM), optical stretching, and magnetic bead cytometry (10-12). While these methodologies have been instrumental in elucidating the molecular basis of cellular mechanics, they require highly skilled operators and sophisticated equipment and, most importantly, suffer from low experimental throughput. For example, AFM and optical stretching techniques have sampling rates on the order of 1 cell per minute (if not slower), which severely reduces statistical power and complicates if not precludes the identification of rare cellular subpopulations. Additionally, many of these techniques require either direct contact between a probe and cell, adhesion to two-dimensional culture substrates, or both, which may invite measurement artifacts.

To address these issues, microfluidic tools have recently been explored as a strategy to measure cellular structural and mechanical properties with a rapidity that may be better suited to

drug discovery and clinical application (13-24). While these approaches have indeed massively improved measurement throughput and reduced operator skill/bias issues relative to traditional measurements, the extraction of cell mechanical properties (e.g. elastic modulus) remains challenging primarily due to complex viscous forces that severely complicate analysis of deformations.

Recently, Guck and colleagues performed rapid cell deformability measurements with a device that squeezed cells into a bullet shape as the cells passed through square constriction channels (18, 19). By using a viscous medium (viscosity $\mu \sim 15$ mPa·s, versus 1 mPa·s for water at room temperature), the device could be operated at low Reynolds number ($Re \sim 0.1$), thereby enabling the development of an analytical model from which elastic moduli of cells could be determined from the resulting deformations (19). While this method has proven quite powerful, it is both analytically demanding and requires accurate edge detection of a complicated shape to extract elastic properties.

In an attempt to achieve high-throughput mechanical measurements within a simpler geometry, Di Carlo and colleagues developed higher-Reynolds number ($Re > 40$) microfluidic systems that measure cell deformability with throughput ranging from 1000 cells/second (14) to 65,000 cells/second (15). By elongating cells at the stagnation point of extensional flow or pinching cells with two sheathing flows, they successfully developed population "signatures" based on distributions of cell deformability vs. size. These population signatures responded in expected ways to cytoskeletal drugs in the pinched-flow sheathing device for which strain rates and imposed cell strains were not too large (15) (the expected effects of cytoskeletal depolymerization drugs were not detected in the high strain rate, high strain extensional flow device (13)) and enabled prediction of disease state from clinical samples (13, 14). Nonetheless, this work did not present an analytical route to extract cell constitutive model parameters, instead requiring numerical solutions due to the high inertial component of the flow. Thus, there remains a significant need for microfluidic strategies to measure cellular viscoelastic properties in a simple geometry subject to well-defined deformation forces.

In this study we present a novel cross-slot microfluidic system that addresses these limitations. By strategically choosing our device geometry and suspending fluid, we are able to greatly simplify both the experimental workflow and mechanical analysis and thereby arrive at a single analytical equation that relates deformation, channel geometry, and cellular viscoelastic parameters. The expected elliptical deformed shape is more easily analyzed and less sensitive to noise in image processing compared to a more complicated shape with rapid changes in curvature. We validate the approach by measuring the elastic properties of cross-linked dextran hydrogel particles, using independent micropipette aspiration measurements and previously published values for stiffness as comparisons. We then apply this system to measure the apparent shear modulus and fluidity (viscosity parameter) of 3T3 fibroblasts and primary glioblastoma tumor initiating cells (GBM TICs) and show that we can capture expected changes in cell stiffness in the presence of specific pharmacologic agents.

MATERIALS AND METHODS

Microfluidic Device Fabrication

Microfluidic cross-slots were fabricated using standard soft lithography. This geometry, consisting of two channels that intersect at 90 degrees, is a convenient platform for generating a

planar extensional flow. Masters for the cross-slots used for the cell experiments were made from SU-8 patterned on silicon wafers following standard soft lithography approaches (25). Briefly, silicon wafers were pre-cleaned with piranha solution (3:1 sulfuric acid to hydrogen peroxide), washed with DI water, and baked at 120°C for 20 minutes to remove any moisture. After spin-coating a 30-µm layer of SU-8 2025 photoresist (Microchem, Boston, MA) onto the wafer, the wafer was exposed to 365-nm UV light at ~40 mW/cm^2 for 12 s under a mylar mask printed with the cross-slot pattern (Artnet Pro, San Jose, CA). After development, wafers were pretreated with trichloro (1H,1H,2H,2H-perfluoroocytl)silane to prevent adhesion of the polydimethylsiloxane (PDMS) to the silicon wafer. PDMS and curing agent (Sylgard 184, Dow Corning, Midland, MI) were mixed in a 10:1 ratio, degassed, and poured over the silicon master. The PDMS was cured overnight at 80°C before the PDMS patterns were removed. Inlet and outlet holes were punched with an 18-gauge blunt needle (McMaster Carr, Elmhurst, IL). The PDMS devices were bonded to glass microscope slides after oxygen plasma treatment, and bonding was finalized by curing the PDMS/glass device in an oven at 80°C overnight. The cross-slot channel geometries for the cell experiments had widths of 70 or 100 µm, a depth of 30 µm, and channel lengths to the cross-slot region of 1 or 2 mm.

For the dextran particle experiments, which required very deep devices, masters were made from dry-film photoresist on stainless steel wafers. Prior to lamination, the steel wafers were rinsed with acetone and water. Two layers of 100 µm-thick dry-film photoresist (Riston GoldMaster GM100 photoresist, DuPont, Research Triangle Park, NC) were laminated onto the steel wafer with the rollers heated to 120°C (Akiles Prolam Ultra, Mira Loma, CA). The dry-film photoresist was exposed to 365-nm UV light at ~40 mW/cm^2 for 10 s under a mylar mask printed with the cross-slot pattern (Artnet Pro, San Jose, CA). The laminate was developed with 10% K_2CO_3 solution and then dried. The PDMS cross-slot devices were prepared from the dry-film photoresist masters in the same manner as from the SU-8 masters. These large devices with 200 µm depth, 400 µm width, and channel lengths of 2 mm, accommodated the large (40-100 µm diameter) dextran hydrogel particles.

Cell Culture

NIH 3T3 mouse fibroblasts (ATCC, Manassas, VA) were cultured on tissue culture plastic in complete medium consisting of Dulbecco's Modified Eage's Medium (DMEM) (Gibco, Carlsbad, CA) with 10% calf serum (JR SCIENTIFIC, Woodland, CA) and 1% penicillin/streptomycin (Gibco). Primary GBM TICs were collected in a previous study after informed consent from male patients who underwent surgical treatment and Institutional Review Board approval (26). The TIC neurospheres were propagated in neurosphere assay growth conditions (27) with serum-free medium (Neurocult NS-A Proliferation kit, Stem Cell Technologies, Vancouver, Canada) supplemented with epidermal growth factor (EGF) (20 ng/ml, R&D Systems, Minneapolis, Minnesota), basic fibroglast growth factor (bFGF) (R&D Systems) and 2 µg/ml heparin (Sigma, St. Louis MO, USA) The gliomaspheres were serially passaged every 5 to 7 days, when the spheres reached a diameter of ~150 µm. Gliomaspheres were dissociated with trypsin/ethylenediaminetetraacetic acid (0.05%) for 2 minutes and then replated in fresh media with the addition of EGF, bFGF, and heparin. Both cell cultures were grown in a humidity-controlled 5% CO_2 incubator at 37°C.

Pharmacologic studies

For studies with cytochalasin D (CytoD), cells were incubated with 10 μM CytoD (Sigma-Aldrich, St. Louis, MO) for 30 minutes prior to the experiment. CytoD was then also added to the suspending solution at 10 μM to ensure exposure to a constant CytoD concentration during cross-slot deformation. For paraformaldehyde (PFA) studies, cells were fixed with 4% PFA (Alfa-Aesar Haverhill, MA) in phosphate-buffered saline (PBS) for 10 minutes in culture and then washed 3 times with PBS to remove any residual PFA prior to resuspension. Because PFA irreversibly cross-links cellular proteins upon transient treatment, it was not necessary to include PFA in the medium during measurement.

Cross-slot Deformation Experiments

Cells and dextran hydrogel particles were suspended in 20% (cells), 30% or 40% (dextran particles) w/v 20000 Da polyethylene glycol (PEG20000)/PBS solution in order to operate in the low Reynolds number regime and to reliably focus the majority of cells/particles during cross-slot deformation. The PEG had a viscosifying effect so that a given fluid stress could be applied at lower fluid velocities to make image capture and analysis of cell and dextran particle deformation easier. The viscosity of the PEG20000/PBS solution was measured at 25°C using an Anton Paar Physica MCR 301 rheometer with a 50 mm parallel plate geometry. The measured viscosities were nearly constant across the tested strain rates (1-2000 s^{-1}): 35 to 50 mPa·s for 20% w/v solutions, ~100 mPa·s for 30% w/v solutions and ~200 mPa·s for 40% w/v solutions (Fig. S1 in the Supporting Material). The high concentration of PEG also increased the density of the suspending solution to 1.03-1.05 g/mL so that cells and dextran particles were approximately neutrally buoyant. Thus, during observation of deformation at the mid-channel height (i.e. 15 μm above the glass bottom surface for cells in the 30 μm deep device), most cells and particles were in focus and candidates for measurement. 3T3 and GBM TIC cells were trypsinized into a single cell suspension and then resuspended in the PEG20000/PBS solution. For cells treated with CytoD, drug at the same concentration as for incubation was included in the solution to prevent recovery of the cytoskeleton from the depolymerization. Typical cell densities were 8-10 million cells/mL as measured by a hemocytometer. The cross-linked dextran beads were Sephadex G200 beads in powder form (GE Healthcare, Little Chalfont, United Kingdom) and were simply added to the PEG20000/PBS solution.

The cell and dextran particle suspensions were loaded into 1 mL syringes (BD Falcon, San Jose, CA). Cell and particle suspensions were infused into the cross-slot device using a syringe pump (Cole-Parmer 74900 series dual syringe pump) at constant flow rates ranging from 50–1400 μL/hr for the cells and 2.5–40 mL/hr for the dextran hydrogel particles. To account for the compliance in the microfluidic device and tubing, the system was allowed at least 2 minutes to equilibrate before data capture after each new flow rate adjustment.

Cells or dextran particles flowing in both cross-slots were elongated at constant strain rate in extensional flow and observed passing through the stagnation point region. Deformation was imaged in phase contrast mode using a Nikon TE2000-E2 microscope with a 40x objective (~2 px/μm), and the plane of focus was the device centerplane. Images were captured by using a high-speed Phantom Miro M310 camera at 2000 frames per second with 20 μs exposure in order to obtain several images per cell or particle, thereby capturing the evolution of the deformation, and to minimize blurring due to cell or particle movement. All movies were captured within 30 minutes of the trypsinization process.

Cell and dextran particle deformation images were analyzed with custom software written for ImageJ (NIH) and Matlab (2013v, Mathworks). Cell strain was defined as $\varepsilon = (a-$

b)/(a+b), where a and b are the long and short axes, respectively, of an ellipse fitted manually to the outer edge of the cell membrane (Fig. 1A, Fig. S3 in the Supporting Material). Our definition of cell strain is equivalent to the Taylor deformation parameter (28) historically used to define droplet deformation (29-31) and adapted to quantify red blood cell deformations (20, 24, 32). The cell strain measurement was taken at the time point in which the cell was closest to the stagnation point. Additionally, this definition of ε is also the magnitude of engineering strain along the x- and y-axes: $\varepsilon = |(R-R_0)|/R_0 = |\Delta R|/R_0$ where the change in sphere radius at the surface is $\Delta R > 0$ along the y-axis (outlet flow axis) and $-\Delta R$ along the x-axis (inlet flow axis). Note that the sphere strain along the z-axis is zero for planar extensional flow due to zero velocity in the z-coordinate direction and therefore no contribution to the velocity gradient that determines the viscous fluid stresses acting on the sphere surface.

Cells were excluded from analysis if one of the following criteria was met:

- The cell was not spherical before entry into the cross-slot, as the analytical model becomes invalid since the assumed initial state for deformation computation is incorrect.
- The cell was not sufficiently centered in the channel width direction (closer than 25% of the channel width to the walls) or was adherent to another object (e.g., another cell), as the analytical model becomes invalid since the object does not experience the assumed strain rate.
- The cell membrane appeared damaged.
- The cell was either very large or very small compared to other cells (for a distribution of the cell size of the analyzed population of cells, see Fig. S4 in the Supporting Material), as these cells may be apoptotic, multinucleated, or otherwise abnormal and empirically demonstrated very large or very small deformations far outside the population average.

The same exclusion criteria applied to dextran hydrogel particles, though the criterion related to the assumed strain rate was the only one that applied in practice because the particles were all initially spherical and intact.

The mechanical properties of cells and dextran particles were determined from the analysis of the deformation due to the known viscous forces. At a given flow rate, cell type, and drug treatment, the reported deformation under those experimental conditions was computed as the average deformation of $10 \leq n \leq 30$ cells with an uncertainty defined as the standard error of the mean. Mechanical property parameters were obtained through linear regression with a least-squares fit of the observed strain ε to cross-slot extensional strain rate $\xi U/D$ (for cells, log-log plot) or viscous stress $\mu\xi U/D$ (for dextran particles, linear plot) based on the theory described in the Results Section where ξ, U, and D are defined. The uncertainties in the linear fits and the significance of the differences in measured material properties between the cell pharmacologic studies are evaluated using analysis of covariance (ANOCOVA).

Micropipette Aspiration Experiments

Micropipettes were fabricated from glass capillaries as described in Guillou et al. (33) and mounted on motorized micromanipulators. The aspiration pressure was applied using an air-filled syringe and determined using a home-made pressure sensor as described in Hogan et al. (34). Aspiration pressure was increased from 0 to 10 kPa by incremental steps of 2 kPa. After each pressure step, an image of the aspirated Sephadex bead was acquired using a 40x objective.

RESULTS

Theoretical analysis of the deformation of an elastic body in a cross-slot device

We begin by calculating the viscous stresses experienced by spherical bodies flowing through the stagnation point region of a cross-slot device and apply these findings to the simple case of an isotropic, linearly elastic spherical particle. Our result is valid in the limit of low Reynolds number flow and small deformations of the particle. Indeed, these two modeling assumptions were met in the upcoming results as we observed cell strains of $0.01 < \varepsilon < 0.18$ under operating conditions in which the flow Reynolds number was small, specifically $0.006 < Re < 0.2$ (range of all experimental parameters given in Table S1 in the Supporting Material). Therefore the effects of fluid inertia can be assumed to be negligible compared to viscous fluid forces and omitted from our model. In contrast, the Reynolds number in the cross-slot devices of Di Carlo and colleagues (13, 15) were finite at operating conditions ($Re > 40$) and therefore fluid inertia would need to be included in the modeling of cell deformation in their system.

Our system parameters are the channel half-width D, the channel height h, the medium dynamic viscosity μ, the fluid density ρ and the mean flow velocity U (see Fig. 1). We define the flow Reynolds number as $Re = \rho UD/\mu$ and consider only the case where $Re << 1$. Hence, viscous forces dominate inertial forces and we assume Stokes flow. The cross-slot generates approximately planar extension flow, in which the velocity field is $\mathbf{v} = \Omega(-x\mathbf{i} + y\mathbf{j})$ and Ω is the uniform extensional strain rate. Therefore, in the stagnation point region under these laminar flow conditions, the velocity gradient is nearly constant. In particular, along the inlet center streamline (x-axis), the velocity gradient is approximately $\Omega = U_{in}/D$, indicating the velocity decreases linearly from U_{in}, the velocity at the entry of the cross-slot region ($|x| = D$), to zero at the stagnation point. Other investigators previously measured this velocity behavior along the center streamline using micro-PIV measurements (35), and we confirmed the uniform strain rate with our own measurements in the device used for the cell experiments (Fig. S8 in the Supporting Material). We introduce the normalized entrance velocity $\xi = U_{in}/U$, and the stagnation point region velocity gradient is $\Omega = U_{in}/D = \xi U/D$. Because U and D are set by the experimental conditions, ξ is the only remaining factor that must be derived to obtain the velocity gradient in the stagnation point region.

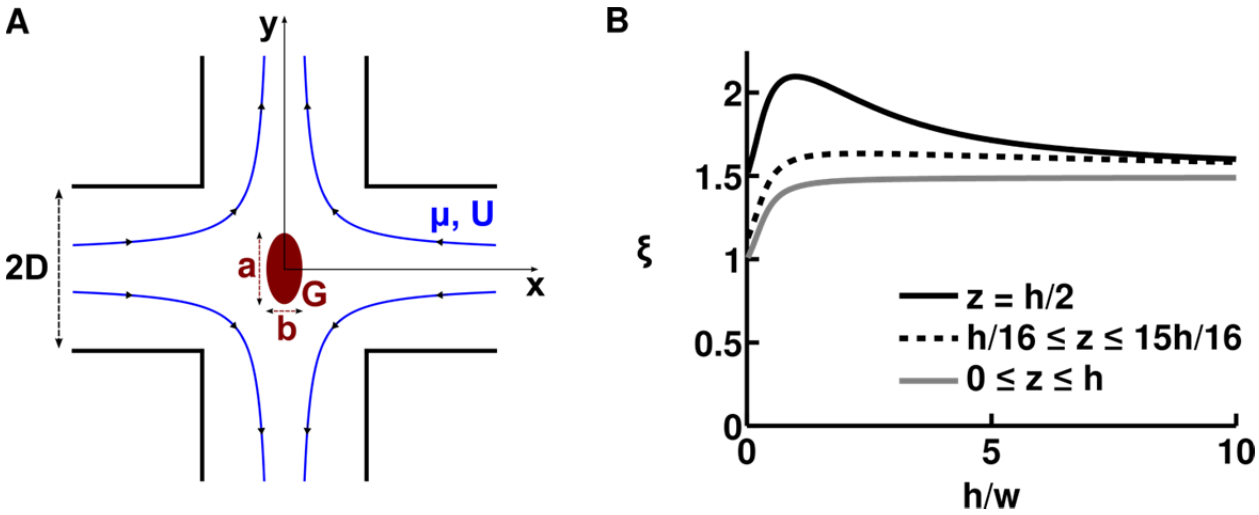

Figure 1. Cross-slot flow field. (A) Cross-slot device containing a body (red) that is initially spherical but then elliptically deforms under elongational viscous fluid stresses (flow streamlines in blue). D is the channel's half-width. a and b, respectively, denote the long and short axes of the ellipse. G is the shear modulus of the body. μ is the fluid dynamic viscosity and U is the mean flow velocity. (B) Normalized entrance velocity $\xi = U_{in}/U$ at the entrance to the cross-slot stagnation point region ($|\mathbf{x}| = \mathrm{sqrt}(x^2 + y^2) \leq D$), as a function of the channel's aspect ratio, A = h/w, where h and w (w = 2D) are the channel height and width, respectively. Values for normalized entrance velocity are computed using our derived analytical expression for ξ_{max} and ξ_{min}. z denotes the position of the vertical axis, with the channel occupying $0 \leq z \leq h$. ξ_{max} is plotted as a black line and corresponds to an object at the vertical center of the channel, where the velocity is maximal. ξ_{min} is plotted as a grey line and corresponds to objects that are in the middle of the channel's width but distributed equally along the height of the channel. The dotted black line indicates an example of the normalized entrance velocity ξ for objects that are in the middle of the channel's width and distributed equally along the height of the channel with the exclusion of the very bottom and the very top of the channel (in this example, we excluded 1/8 of the total channel height). This final value (dotted black line) is the one that best matches experimental observations.

In a first step, we restrict our analysis to the position of maximal in-plane (x-y) velocity gradient, corresponding to an object that is at the channel's vertical center (z = h/2) and in the middle of the channel's width (y = 0) where $U_{in} = U_{max}$. In such a case, $\xi = \xi_{max} = U_{max}/U$. Using the known velocity profile for laminar flow through a rectangular channel (36), we are able to derive an analytical expression for ξ_{max} in terms of a Fourier series in the channel aspect ratio A = h/(2D) = h/w:

$$\xi_{max} = \frac{3/2 - 6\sum_{n=0}^{\infty} \frac{(-1)^n}{\lambda_n \cosh(\lambda_n / A)}}{1 - 6A\sum_{n=0}^{\infty} \frac{\tanh(\lambda_n / A)}{\lambda_n^5}} \qquad \text{where } \lambda_n = \frac{(2n+1)\pi}{2} \qquad \text{(Equation 1)}$$

We note that for A < 1, both infinite series in Eq. 1 can be approximated by their first term with an error for ξ_{max} of less than 1%. For 1 < A < 3, one must add the second series term to maintain an error of less than 1%. Further, we verified that in the quasi-2D limit where A goes to 0 (corresponding to a very flat channel), ξ_{max} converges to 3/2, the well-known maximum-to-mean velocity ratio in a 2D parabolic flow. We also note that because inverting the width and height does not affect the maximum nor the mean velocity, $\xi_{max}(A) = \xi_{max}(1/A)$.

In a second step, we relax the constraint that the body must be located at the channel mid-height because it is difficult to perfectly focus all cells in experiments. Still assuming that the body is at the center of the channel width direction, the body may now be located anywhere on the vertical axis so that $U_{in} = U_{w/2}$. We use the same approach as above, and derive the normalized velocity $\xi_{min} = U_{w/2}/U$ in terms of a Fourier series:

$$\xi_{\min} = \frac{1 - 6A\sum_{n=0}^{\infty} \frac{1}{\lambda_n^{\,4}\cosh(\lambda_n / A)}}{1 - 6A\sum_{n=0}^{\infty} \frac{\tanh(\lambda_n / A)}{\lambda_n^{\,5}}} \qquad \text{where } \lambda_n = \frac{(2n+1)\pi}{2} \qquad \text{(Equation 2)}$$

$\xi_{\min}$ is plotted for aspect ratios between 0 and 10 in Fig. 1B (solid grey line). We note that for A < 1, both infinite series in Eq. 2 can be approximated to their first term with an error for $\xi_{\min}$ of less than 1%. For 1 < A < 3, one must add the second series term to maintain an error of less than 1%.

In experiments, objects were predominantly near the mid-plane of the channel, so ξ assumed values that lie between $\xi_{\min}$ and $\xi_{\max}$. To further refine the expression for the experimental value of ξ, we adjust Eq. 2 to take into account the radius of the object being deformed, in which case we find that the normalized velocity is almost always close to 1.5 (see Fig. 1B, Supporting Results for more details), except for high aspect ratio channels that are seldom used in microfluidics, in part because objects will often be out of focus as a consequence. For simplicity, we retain this value of 1.5 in our subsequent experimental analysis. Thus, the velocity gradient in our device is $\Omega = \xi$ U/D, where ξ is expressed analytically as a function of the aspect ratio A = h/w of the device. In the experiments reported here, $\xi \sim 1.5$.

By scaling arguments and analysis of the cross-slot flow field, we can therefore reasonably assume that objects sufficiently close the stagnation point are deformed by our derived strain rate ξ U/D. The results for ξ are derived in the absence of cells or particles. We verified that the size of cells was sufficiently small to avoid perturbations to the flow as evidenced by the small value of the Stokes number Stk ~ 10^{-6} << 1 (see details in Supporting Results and Fig. S7 in the Supporting Material). Our Hele-Shaw simulation results of the cross-slot flow field and our micro-PIV measurements (Fig. S8 in the Supporting Material) as well as other reported particle image velocimetry measurements (Ref. (37) Fig. S2, Ref. (35) Fig. 5D) indicate that the strain rate is constant in the stagnation point region. According to our Hele-Shaw simulations, for distances smaller than 25% of the channel width away from the stagnation point, the local strain rate is within 95% of the maximum value at the stagnation point (Fig. S2 in the Supporting Material).

Having characterized the velocity gradient in the device, we consider the simple case of an isotropic, linearly elastic material deforming in a pure and infinite planar extensional flow. Murata (38) analyzed the general problem of an incompressible elastic sphere deforming in an arbitrary, low Reynolds number flow field in the limit of small deformations (ε << 1). From Murata's example solution for the surface of a sphere deforming in planar extensional flow, we obtain the following relation for the strain in this flow field: $\varepsilon = (5\Omega\mu)/(2G)$, where G is the shear modulus and the strain is defined as ε = (a-b)/(a+b) (Fig. 1A). Plugging in our expression for the velocity gradient Ω, we find an expression for the strain of an elastic sphere deforming in our cross-slot device:

$$\varepsilon = \frac{a-b}{a+b} = \frac{5}{2}\xi\frac{U}{D}\frac{\mu}{G} \qquad \text{(Equation 3)}$$

Extension of the theory to the deformation of a viscoelastic body in a cross-slot device

We next extend the relation to the deformation of a viscoelastic body in planar extensional flow. Because the fluid velocity gradient is uniform in a cross-slot and because the fluid forces exerted

on a cell are largely dominated by viscous forces that are proportional to this homogenous velocity gradient, a body moving through the cross-slot's central region ($|\mathbf{x}| \leq D$) will be submitted to viscous stresses proportional to $\tau \sim \mu \dot{\xi}$ U/D, assuming the disturbance to the velocity field due to the presence of the cell is small (see details in Supporting Results). While for an elastic body, the uniform viscous stresses means an instantaneous and constant deformation, the deformation of viscoelastic bodies such as suspended cells changes with time under loading by a constant stress and depends not only on the force magnitude but also the rate at which the force is applied. One choice of model to capture viscoelastic behavior is the simple two-parameter power law for a time-dependent cell stiffness. This phenomenologic law has been shown to describe cell mechanical behavior for several cell types over a wide range of time scales as measured by several techniques including optical magnetic twisting cytometry (39, 40), atomic force microscopy indentation (41), and microfluidic constriction channel traversal (17). The power law can be expressed mathematically as follows (39):

$$G(t) = G_0 \left(\frac{t}{t_0} \right)^{-\alpha} \quad \text{(Equation 4)}$$

where t_0 is an arbitrary reference time, G_0 is the value of the shear modulus at time t_0, and the fluidity parameter α describes the dependence of the shear modulus on time. The case of a purely elastic body is recovered by choosing $\alpha = 0$, and a Newtonian fluid corresponds to $\alpha = 1$. For a viscoelastic material with $0 < \alpha < 1$, the power-law model predicts that as the deforming force is applied more quickly (smaller t), the material appears stiffer (larger G(t)). A rigorous implementation of this relaxation modulus G(t)—the viscoelastic, time-dependent analog of the shear modulus G for an elastic material—requires a more complicated stress-strain relationship involving an integral in time. This constitutive law would need to be incorporated into the time-dependent version of the governing equations for the solid undergoing infinitesimal deformations, which are more complicated than the steady-state versions used to derive Eq. 3. In a simplistic approach, we will not explicitly consider the time-dependent modulus G(t) in the governing equations, but rather consider the cell to be an elastic sphere with an 'effective' shear elastic modulus $G(t_{cs})$, where $G(t_{cs})$ is G(t) evaluated at the time-scale t_{cs} of cross-slot deformation. Thus we have taken a phenomenological approach as opposed to a rigorous mechanics derivation by replacing G in Eq. 3 by $G(t_{cs})$. We show below that, despite these simplifications, this power-law adequately describes our own measurements of suspended cells.

We observed the deformation of single cells at the time point nearest to the stagnation point and thus extract the time-dependent shear modulus at a certain time after the start of deformation. By varying the flow rate, we sample a range of deformation times and strain rates. Using our knowledge of the well-defined extensional flow field, we calculate the average time of deformation at a given flow rate experienced by the cells as they travel from the end of the channel towards the stagnation point. This time of deformation is expected to scale with D/U. By symmetry, we considered the upper quadrant of the cross-slot defined by $x > 0$ and $y > 0$. When entering the cross-slot, the body travels at a velocity of the extensional flow field $\mathbf{v} = u\mathbf{i} + v\mathbf{j}$ where $u(x) = -\Omega x$ and $v(y) = \Omega y$. Therefore, choosing $t = 0$ to be the point in time where the body enters the cross-slot region at $|x| = D$ and starts being exposed to the extensional stresses, integration along the streamline yields the x coordinate of cell position to be $x = D \exp(-\Omega t)$. This is equivalent to a time of extensional deformation $t = -1/\Omega \ln(|x/D|)$ for an object that started at $x = D$ at $t = 0$ and is now located at a new $x < D$ after flowing entrained in the extensional flow

field. We restrict the analysis to bodies whose centers are located in the region where x ϵ [0;D/2] and y ϵ [0;D/2], equivalent to our experimental criteria that bodies are imaged close to the stagnation point. The average time of deformation for cells observed in the region x,y ϵ [0, D/2] is therefore:

$$t_{cs} = \frac{-1}{D/2}\int_0^{D/2} \frac{1}{\Omega}\ln\left(\frac{x}{D}\right)dx = (1+\ln(2))/\Omega \qquad \text{(Equation 5)}$$

This equation yields the expected scaling with D/U, apparent when rewritten as t_{cs} = (1+ln(2))D/(ξ U). Notwithstanding this result, we note that any other choice of zone is possible; both derivation methods for the normalized velocity ξ and the time spent in the cross-slot t_{cs} would have remained valid and would have just led to different final equations. For instance, choosing the entire cross-slot would have led to $t_{cs} = 1/\Omega$.

This derivation of t_{cs} assumes that the cell travels at the fluid velocity. We performed several particle-tracking measurements and found that, within experimental error, cells traveled close to the expected maximum fluid velocity (see Fig. S9 for details). Our results are supported by theoretical and simulation results from Guck and colleagues showing that objects travel at >90% of the maximal fluid velocity when the degree of confinement is $r_{cell}/R_{eq} < 0.4$ where r_{cell} is the cell diameter and R_{eq} is the equivalent channel radius (Ref. (19) Fig. 2A). Defining R_{eq} based on hydraulic mean radius of our rectangular channels (R_h = 23 μm), these results predict that cells with diameter r_{cell} < 9.2 μm travel at >90% of the maximal fluid velocity. Thus r_{cell} < 9.2 μm is an upper bound on cell size for the range of applicability of our model. The histograms of cell size presented in Fig. S5 in the Supporting Material show that the cells measured are below this upper bound with an average cell radius around 7 μm.

Combining Eqs. 3, 4 and 5, we present the following analytical relation that relates the observed body deformations with the cross-slot dimensions, the suspending fluid viscosity, and the applied flow rate via two fitting parameters, α and G_0, that describe the body's viscoelastic behavior:

$$\varepsilon = \frac{5}{2}\frac{\mu}{G_0}\left(\frac{1+\ln(2)}{t_0}\right)^{\alpha}\left(\frac{\xi U}{D}\right)^{1-\alpha} \qquad \text{(Equation 6)}$$

G_0 corresponds to the apparent stiffness for a given time t_0. In our analysis of cell deformation, we will choose t_0 = 5 ms, the average t_{cs} across all cell experiments, as a time scale that is naturally suited for the apparent stiffness.

Experimental validation of the deformation of an elastic body in a cross-slot device

In order to experimentally assess the validity and accuracy of the model, we performed studies on a model elastic body whose mechanical properties had been previously determined using other systems. Our theory required that this body be initially spherical and that it deforms at low Reynolds number. We chose Sephadex G200 cross-linked dextran beads with diameters ranging from 40 to 100 μm, which are the most deformable of all commercially available Sephadex beads due to their large porosity. These particles are spherical in a stress-free state and deformed in cross-slot experiments operated at low Reynolds number (0.001 < Re < 0.1). Our experimental

system required that the average flow velocity U be less than ~0.18 m/s, as velocities above this value precluded accurate tracking of deformations.

We introduced Sephadex G200 beads into our cross-slot device and observed deformations in the vicinity of the stagnation point (Fig. 2A). Since with the employed magnification, a Sephadex bead is typically 50 to 100 pixels in diameter, the lowest strains (engineering strains) detectable for an individual Sephadex is of the order of 1% (the fitting of an ellipse rounds up or down to the nearest pixel). By employing solutions of varying viscosities (105, 179, and 201 mPa·s) and flow rates (2.5–40 mL/hr), we sampled a wide range of strain rates (ξ U/D ~ 65–1300 s^{-1}). As predicted by Eq. 3, the mean particle deformation was linearly related to the applied stress, with a shear modulus (slope) of G = 8.6 ± 0.5 kPa (Fig. 2B).

We then validated these stiffness measurements by performing micropipette aspiration experiments on the same Sephadex G200 beads in the same suspending PEG/PBS medium (Fig. 2C). Application of linear elasticity theory (42) to relate the entry length of the dextran beads inside the micropipette with the aspiration pressure yielded shear moduli of G_{asp} = 6.4 ± 0.2 kPa. This is in reasonable agreement with our cross-slot measurement and in order-of-magnitude agreement with previous measurements by osmotic deswelling (43) and suspension rheology (44) (Fig. 2D). Microscale mechanical measurements are expected to be more sensitive than bulk measurements to microscopic structural inhomogeneities, such as defects or variations in cross-linking density (45). This means that measured values are quite sensitive to the method of force application. For instance, localized application of force (aspirate one region of particle in MPA) could be expected to give different results than more homogenous applied forces (elongation in a uniform velocity gradient in cross-slot microfluidic device) that may present a more averaged response that masks microparticle structural inhomogeneity. Furthermore, each method makes simplifying assumptions in order to extract material properties from primary measurements such as deformation, thereby introducing systematic error that is not included in reported measurement uncertainty, typically a population standard deviation or standard error of the mean.

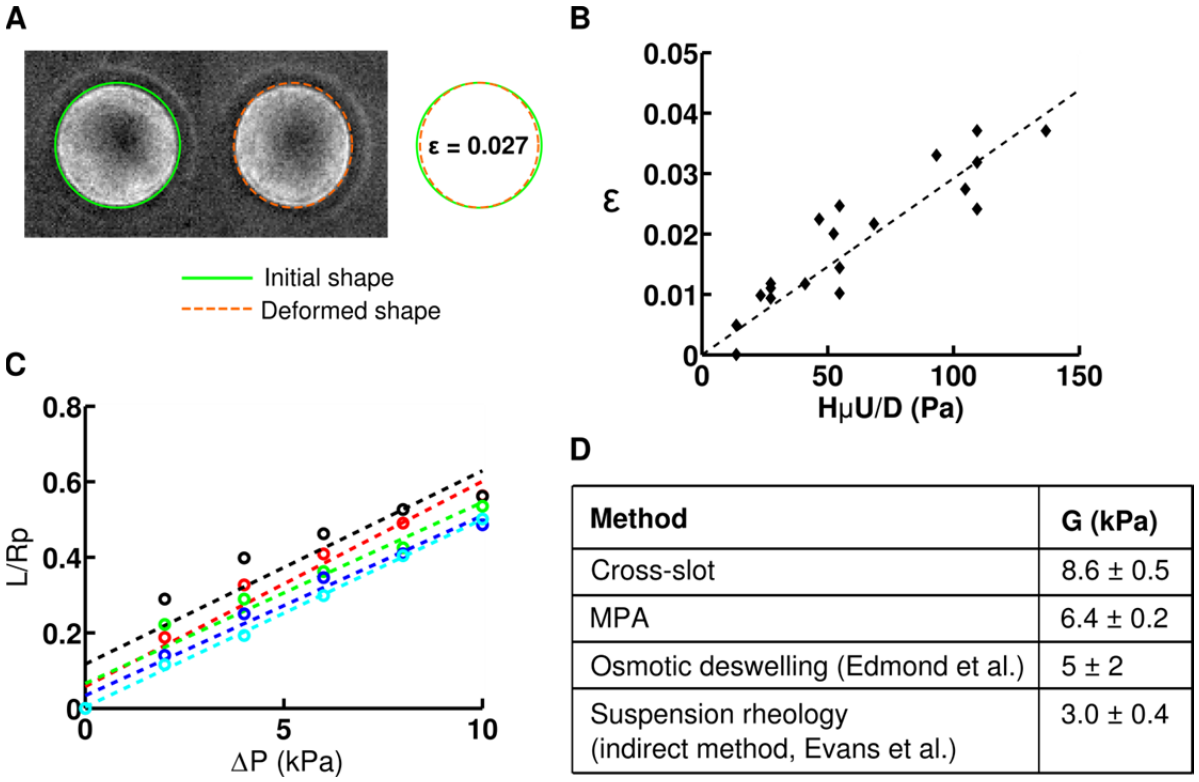

Method	G (kPa)
Cross-slot	8.6 ± 0.5
MPA	6.4 ± 0.2
Osmotic deswelling (Edmond et al.)	5 ± 2
Suspension rheology (indirect method, Evans et al.)	3.0 ± 0.4

Figure 2. Validation of cross-slot mechanical measurements with cross-linked dextran hydrogel particles. (A) Time-lapse of a Sephadex G200 cross-linked dextran particle stretching in extensional flow as it passes through the stagnation point region. The shear modulus is extracted from the observed deformation. Cross-slot dimensions are 400 μm wide and 200 μm deep. The strain rate is $\xi U/D \sim 520\ s^{-1}$ at 20 mL/hr flow rate. Right: Overlay of the ellipses manually fitted to images of the dextran particle at the entrance of the cross-slot region and at the location closest to the stagnation point. The deformation was chosen to be an average case of all observed deformations. (B) Deformation of Sephadex G200 beads as a function of the applied stress. Suspending fluids with three viscosities were used, μ = 105 mPa·s, 179 mPa·s and 201 mPa·s. A linear regression of $\varepsilon = 5\,\xi\,\mu U/(2GD)$ provides the shear modulus of G = 8.6 ± 0.5 kPa. Reported uncertainties of our measurements are the standard errors of the mean values of the population of dextran beads. (C) Micropipette aspiration of Sephadex G200 beads. The entry length L is normalized by the micropipette radius R_p and plotted as a function of the applied pressure ΔP. Each color represents a different bead (n = 5 beads), and the shear modulus is inversely proportional to the slope. (D) Comparison of shear modulus values obtained with our cross-slot measurements, our micropipette aspiration (MPA) measurements, and previously published values based on osmotic deswelling (43) and suspension rheology (44).

Measuring the viscoelastic properties of 3T3 and GBM TICs

Having validated our analysis and experimental platform, we progressed to measuring mechanical properties of living cells. For proof-of-principle studies, we focused on NIH 3T3 fibroblasts, which have been mechanically characterized by AFM (46, 47), optical stretching (48, 49), and MPA (50). To explore the potential of our cross-slot device for novel discovery, we also characterized GBM TICs, a stem-like subpopulation of GBM tumors thought to drive tumor

initiation, recurrence and therapeutic resistance (26, 51, 52). Importantly, manipulation of mechanics and mechanotransductive signaling in GBM TICs was recently shown to significantly reduce tissue invasion and extend survival (53).

Our model's assumption that the deforming body is initially spherical is a reasonable approximation for cells in suspension in general (54), and for circulating white blood cells in particular (55, 56). For a subset of cells, we measured a deformation (mean ± standard error of the mean) of ε = 0.0004 ± 0.004 (n = 21,) and ε = 0.007 ± 0.003 (n = 28) for 3T3 and GBM TICs, respectively, before entry into the central region of the cross-slot (each sample set taken from two separate experiments on two different days). As another measure of cell sphericity, we also evaluated cell circularity index, defined as $c = 4\pi A/(P^2)$ where A the cell area and P the cell perimeter. (A value of c = 1 indicates a perfect circle while a value of c = 0 indicates a line.) From the ellipses manually fitted to the same subset of cells, we found c = 0.998 ± 0.001 and c = 0.998 ± 0.001 for 3T3 and GBM TICs, respectively, showing that cells are spherical before entering the cross-slot central region.

In separate experiments, we infused both cell types through the device at various flow rates (50–1400 μL/hr) that produce a wide range of strain rates (ξ U/D ~ 280–6800 s^{-1}) and imaged cellular deformations at the stagnation point as with the Sephadex particles (Fig. 3A). We found that the deformation agreed well with the power-law model in Eq. 6, as demonstrated by the linearity of the log-log plots of cell strain ε vs. cross-slot velocity gradient ξ U/D (Fig. 4B and 4C). This relationship continued to hold when we independently varied cross-slot width (w = 2D), fluid viscosity (μ), and flow rate (determines average flow velocity U = Q/A), which are the three tunable parameters in the power-law model (Fig. 3B).

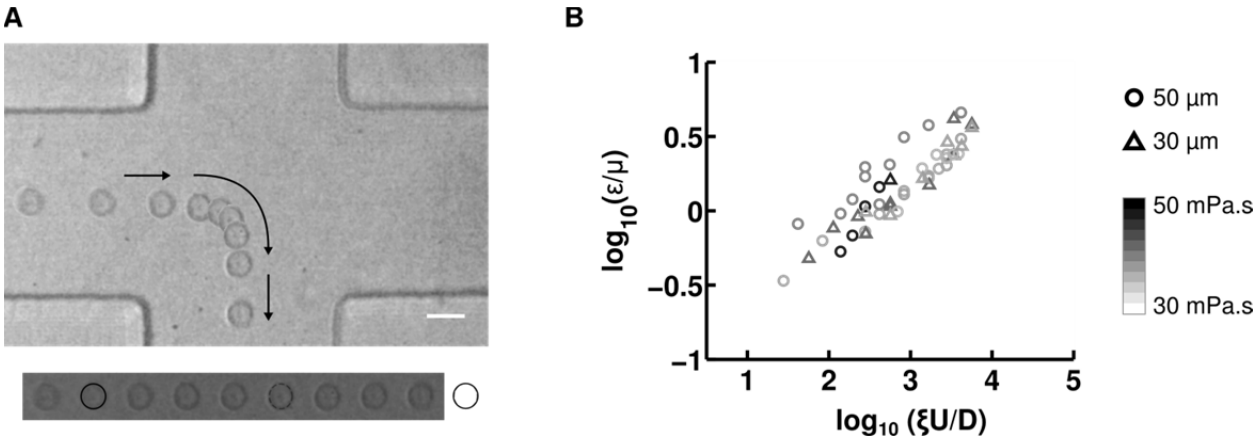

Figure 3. Measurement of cellular viscoelastic properties. (A) Time-lapse images of a 3T3 fibroblast stretching in extensional flow as it passes through the stagnation point region. Arrows denote the direction of movement. Viscoelastic power-law constitutive model parameters are extracted from the observed deformation. Cross-slot dimensions are 100 μm wide, 30 μm deep and the strain rate is ξU/D ~ 1690 s^{-1} at 500 μL/hr flow rate. The time between images 0.5 ms, and the scale bar is 20 μm. We can observe that cell deformation increases as cells pass through the central region of the cross-slot, as is further detailed in Fig. S5. (B) Control TIC cross-slot deformation at various flow rates in devices of varying dimensions and for different suspending fluid viscosities. Each data point represents a separate experimental condition, with $10 \leq n \leq 30$ fitted for the reported average deformation. Marker color indicates fluid viscosity μ

using a grey scale (from white: 30 mPa·s to black: 50 mPa·s) while pattern indicates cross-slot half-width D (triangle: 35 μm, circle: 50 μm). Flow rates varied between 10 μL/hr and 1000 μL/hr. Height was kept constant at 30 μm.

The power law relationship in Eq. 6 predicts that a log-log plot of viscosity-normalized strain (ε /μ) vs strain rate (ξ U/D) would be linear and may be fitted to extract the cellular shear modulus (G) and fluidity parameter (α). Accordingly, for 3T3 cells, we obtained a shear modulus of $G_0(t_0) = 0.59 \pm 0.05$ kPa (Fig. 5) for $t_0 = 5$ ms. Previous measurements on suspended 3T3 cells using optical stretchers yielded shear moduli of ~70-80 Pa (Ref. (49) extracted from Fig. 2A and 3B) and 100 ± 10 Pa (Ref. (48) Fig. 2) for a deformation time scale of t = 200 ms. In turn, if we set our time scale t_0 to 200 ms in our cross-slot experiment, we find that $G_0(200\text{ ms}) = 101 \pm 8$ Pa, which is very consistent with the values found using an optical stretcher. For GBM TICs, we measured a stiffness of $G_0(t_0) = 0.44 \pm 0.03$ kPa. Again, this value is in close proximity to previous AFM measurements on this same cell line that found values of 0.8-0.9 kPa (53). The measured cell fluidity parameter was similar for both cell types: $\alpha = 0.48 \pm 0.04$ for 3T3 cells and 0.50 ± 0.04 for TICs.

We next explored the sensitivity of the measurement to perturbations of cytoskeletal assembly and mechanics. For our softening studies, we used CytoD (10 μM), which has been previously shown to disrupt the 3T3 actin cytoskeleton (57, 58). As expected, inhibition of actin polymerization by treatment with CytoD increased cellular deformation at all strain rates and reduced shear modulus (0.40 ± 0.05 kPa for 3T3 cells and 0.22 ± 0.04 for TICs). Those values are statistically significantly different from the control case, with $p \leq 0.01$ between all groups (see Table S2 in the Supporting Material for individual p-values). Conversely, covalent crosslinking of cells with PFA increased the shear modulus (0.93 ± 0.08 kPa for 3T3 cells and 0.73 ± 0.05 for TICs). Here also, the values were statistically different from the control case, with $p \leq 0.01$ between all groups. Despite these changes in stiffness, neither CytoD nor PFA produced statistically significant changes in fluidity for either cell type.

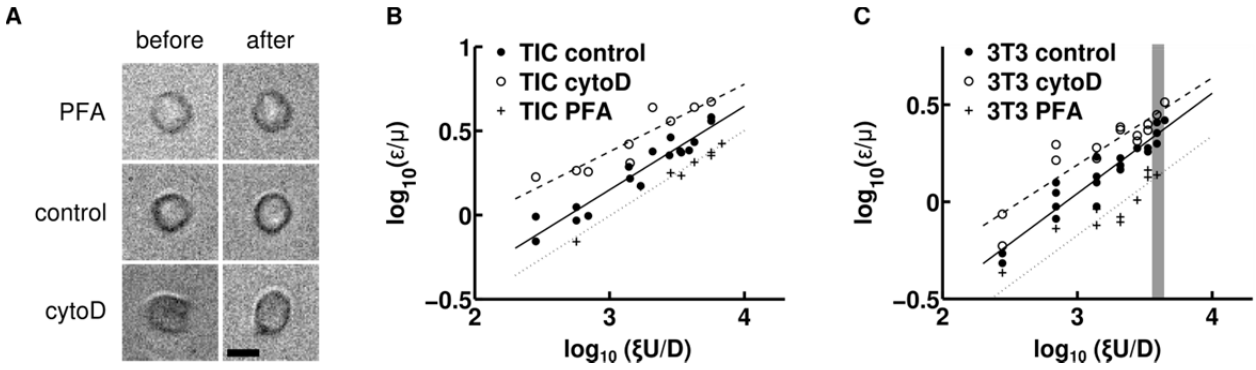

Figure 4. Softening and stiffening effects of drugs that affect the cytoskeleton on TIC and 3T3 deformations measured in the cross-slot. (A) Images of 3T3 fibroblasts before (left) and after (right) deformation by the extensional flow in the cross-slot. We took a cell from all three cases: incubation in PFA (top), control (middle) and incubation in cytochalasin D (bottom). In all three cases, $\xi U/D \sim 4100\ s^{-1}$. Cells were chosen to be representative of the average deformation at this strain rate. The scale bar is 10 μm (B, C). Linear regression of the log-log plots based on ε =

5ξμU/2GD (— solid lines control, -- dashed cytoD, … dotted PFA) yield the cell power-law material properties under control and drug conditions: the fluidity parameter α is obtained from the slope and the shear modulus G_0 at a specified time scale $t_0 = 5$ ms is obtained from the intercept. The cross-slot deformation of both GBM TICs (B) and 3T3 fibroblast cells (C) are consistent with the power-law model as indicated by the linearity of the log-log plots. Each data point represents a separate experimental condition (i.e. ξU/D strain rate and drug condition), with $10 \leq n \leq 30$ cells fitted for the reported average deformation. In panel (C), the grey zone corresponds to the strain rate chosen for the cells in panel (A). For clarity, error bars reflecting the uncertainty in strain measurements (standard error of the mean) is omitted. See Fig. S6 for versions of (B,C) with vertical error bars and Table S3 in the Supporting Material for the cross-slot extensional strain rate (ξU/D), strain (ε) and strain uncertainty for each point plotted in (B, C).

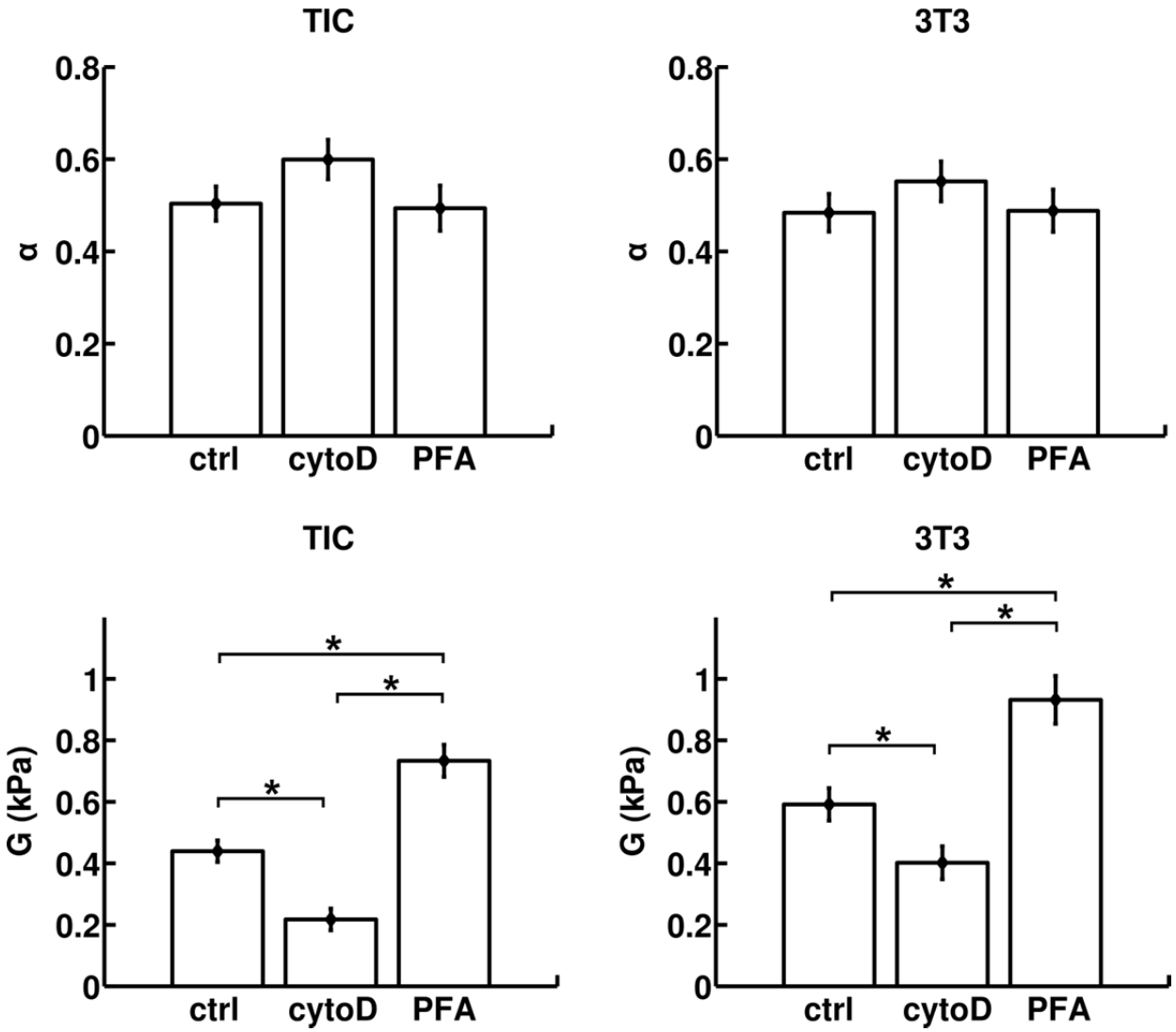

Figure 5. Power-law material parameters, the fluidity parameter α and the shear modulus $G = G_0(t_0)$, evaluated at the average time scale of cell cross-slot deformation $t_0 = 5$ ms for GBM TICs

and 3T3 fibroblasts under different pharmacological interventions. The values of α and G are determined by linear regression and the error bars are derived from analysis of covariance (ANOCOVA). While the fluidity of the cells does not change appreciably, CytoD significantly softens and PFA significantly stiffens both cell types (*$p \leq 0.01$).

DISCUSSION

Cellular mechanical properties serve as a powerful and promising label-free marker for gaining insight into molecular changes within the cell or characterizing different cellular states for potential diagnostic information. Recent advances in microfluidic technology have allowed the high-throughput measurement of cellular mechanical properties with single cell resolution. Such platforms are strongly positioned to detect potential differences in rare subpopulations of cells that may drive disease progression, which would otherwise be masked in bulk- or population-based mechanical measurements. In order to improve on previous studies, we have developed an analytical equation for a simple PDMS-based microfluidic platform to measure and quantify cellular mechanical properties. The strength of our model lies in its simplicity, with a single equation that uses easily obtainable parameters, as well as its adaptability, as it can be readily extended to account for other viscoelastic material laws.

It is interesting to note that while at least one previous study (13) has successfully captured changes in stiffness and correlated these differences to phenotype, it did not report changes in stiffness when cells were treated with cytoskeletal depolymerization drugs. The authors hypothesized that this may be because the high strain rates in their system (ξ U/D ~ $2 \cdot 10^5$ s^{-1}) effectively fluidize the cytoskeleton and are instead dominated by the viscous properties of the cytosol and chromatin. Consistent with this explanation, the lower strain rates employed in our device ($300 \leq \xi$ U/D ≤ 7000 s^{-1}) and many other single cell platforms (e.g. optical tweezers) would facilitate measurement of cytoskeletal mechanics. Key to achieving this regime is our use of high-viscosity fluid medium ($\mu \sim 40$ mPa·s), which enabled us to achieve similar stresses and cellular deformations at much lower strain rates similar to Guck and colleagues who used a viscosified suspending solution of $\mu = 15$ mPa·s (19). Another factor that may contribute to the ability to detect the effects of cytoskeletal depolymerization drugs is the magnitude of cell strain. A different high-throughput device from Di Carlo and colleagues (15) extended cells asymmetrically with pinching sheathing flows so that the leading edge of the cell experienced higher shearing stresses than the trailing edge operated at similar strain rates (ξ U/D ~ $1 \cdot 10^5$ s^{-1}, though a less accurate estimate because the flow is not pure extensional flow) as their cross-slot device in Ref. (13) but deformed the cells less. The high-strain-rate cross-slot device in Ref. (13) deformed cells to strains of $\varepsilon \sim 0.32$ for control and depolymerization drug treated cells while the pinched-flow stretching device in Ref. (15) deformed control cells to $\varepsilon \sim 0.15$ and treated cells to $\varepsilon \sim 0.2 – 0.3$. Our high-viscosity cross-slot system only deformed cells up to a maximum $\varepsilon = 0.18$, a relatively small strain. Consequently, we were able to detect the effect of both softening (CytoD) and stiffening (PFA) interventions in two different cell lines. Moreover, these interventions did *not* significantly change cell fluidity, further consistent with the notion that the strain rates we imposed were insufficient to fluidize the cytoskeleton.

Although our stiffness measurements of both the Sephadex beads and 3T3 cells are of the same order of magnitude as previously published results, there is still a slight variation among all the values, as well as among previously published results. These variations may be due to

differences in measurement modalities across these reports. While the cross-slot platform measures the deformation on a 1-10 ms time scale, the other methods employed (AFM, MPA, osmotic de-swelling and suspension rheology) are performed on a 1-10 second time scale. Additionally, previous measurements have shown that Sephadex bead stiffness increases by ~30% when decreasing the deformation time scale from 10^4 to 10 seconds (44). Hence, we speculate that when decreasing the time scale further from 1 second to 1-10 ms, one would expect some moderate stiffening to occur.

Similarly, for 3T3 cells, reduced time scales unsurprisingly seem to lead to higher apparent stiffnesses. Indeed, in another study, a millisecond-time scale platform measured higher cellular stiffness values than did AFM, which typically involves measurements on the time scale of seconds (59). In the future, it would be valuable to measure bead or cellular mechanical properties across various time scales within the same device. These studies would clarify the exact relationship between the time scale of measurement and the resulting values. Modulation of the viscosity of the suspension medium within our device, as well as the flow rate and the device dimensions, may offer the opportunity to systematically explore these time scales.

We also note some differences in cell deformation behavior in pure extensional flow in a cross-slot compared to previous observations of red blood cell deformation in extension-dominant but non-zero shear flows in a converging-width channel. In a channel converging linearly from large (100 μm wide) to small (20 μm wide) widths over a downstream distance of 70 μm (height a constant 40 μm), four modes of deformation were observed for cells at different cross-stream positions: stretching, twisting, tumbling, and rolling (23). The stretching mode occurred for red blood cells on the channel centerline where the velocity gradient was symmetric about the cell. In our study, although we did observe rolling of cells with visible defects in the entrance channels of the cross-slot device (shear dominant Poiseuille flow), we never observed tumbling or rolling in the stagnation point region (pure extensional flow), only stretching. The existence of one deformation mode in extensional flow -stretching- is expected from cell-mimetic vesicle simulations (60, 61) and experiments (37, 62). Thus, the differences in our observation of one deformation mode compared to the previous four modes of deformation are a result of the different flow fields. In our cross-slot system, the close proximity of the top and bottom walls of the 30-μm-deep channel prevents pure planar (z-independent) extensional flow. However, our observations that cells only stretch near the stagnation point indicates that any shear velocity gradient effects due to the top and bottom walls contribute negligibly to cell deformation. This stands in contrast to the study described earlier in which four modes of deformation were observed (23), which featured significant, non-zero shear components in straight, narrow regions of the channel downstream of the extension-dominant converging section.

CONCLUSION

We have developed an experimental and analytical strategy to measure cellular mechanical properties based on deformations within a microfluidic cross-slot device. By creating measurement conditions that reduce strain rates and developing an analytical model, we successfully detected perturbations to cytoskeletal assembly and mechanics, which is a significant innovation for cross-slot-based systems and enables comparison with more traditional single-cell mechanics measurements. We envision that this technology will prove valuable for the rapid mechanical characterization of living cells in suspension, thereby accelerating

fundamental studies of cellular mechanics and establishing a platform for future diagnostic technologies.

AUTHOR CONTRIBUTIONS

S.J.M., S.K., L.G., J.B.D. and J.G.L. designed research; L.G., J.B.D. and J.G.L. performed research; A.I.B., J.H., S.J.M. and S.K. supervised research; L.G., J.B.D. and J.G.L. analyzed data; all authors wrote the manuscript.

ACKNOWLEDGEMENTS

The authors declare no conflict of interest. Lionel Guillou is supported by a Gaspard Monge fellowship from the Ecole Polytechnique. This material is based upon work supported by the National Science Foundation Postdoctoral Research Fellowship in Biology under Grant No. 1308051 to J.B.D. The work was also supported by grants from the National Science Foundation (105539 to S.K., 1066334 to S.J.M.), the National Institutes of Health (1R01NS074831, 1R21CA174573, 1R21EB016359 to S.K., T32GM098218 training grant support to J.G.L.), the W.M. Keck Foundation (Science and Engineering Grant to S.K.), the Cancer Research Coordinating Committee (fellowship to J.G.L), and a permanent endowment in cardiovascular cellular engineering from the AXA Research Fund.

REFERENCES

1. Ulrich, T.A., E.M. de Juan Pardo, and S. Kumar. 2009. The Mechanical Rigidity of the Extracellular Matrix Regulates the Structure, Motility, and Proliferation of Glioma Cells. Cancer Res. 69: 4167–4174.

2. Rubashkin, M.G., G. Ou, and V.M. Weaver. 2014. Deconstructing Signaling in Three Dimensions. Biochemistry. 53: 2078–2090.

3. Engler, A.J., S. Sen, H.L. Sweeney, and D.E. Discher. 2006. Matrix Elasticity Directs Stem Cell Lineage Specification. Cell. 126: 677–689.

4. Hung, W.-C., S.-H. Chen, C.D. Paul, K.M. Stroka, Y.-C. Lo, J.T. Yang, and K. Konstantopoulos. 2013. Distinct signaling mechanisms regulate migration in unconfined versus confined spaces. J. Cell Biol. 202: 807–824.

5. Bissell, M.J., D.C. Radisky, A. Rizki, V.M. Weaver, and O.W. Petersen. 2002. The organizing principle: microenvironmental influences in the normal and malignant breast. Differentiation. 70: 537–546.

6. Paszek, M.J., N. Zahir, K.R. Johnson, J.N. Lakins, G.I. Rozenberg, A. Gefen, C.A. Reinhart-King, S.S. Margulies, M. Dembo, D. Boettiger, D.A. Hammer, and V.M. Weaver. 2005. Tensional homeostasis and the malignant phenotype. Cancer Cell. 8: 241–254.

7. Levental, K.R., H. Yu, L. Kass, J.N. Lakins, M. Egeblad, J.T. Erler, S.F.T. Fong, K. Csiszar, A. Giaccia, W. Weninger, M. Yamauchi, D.L. Gasser, and V.M. Weaver. 2009.

Matrix Crosslinking Forces Tumor Progression by Enhancing Integrin Signaling. Cell. 139: 891–906.

8. Egeblad, M., M.G. Rasch, and V.M. Weaver. 2010. Dynamic interplay between the collagen scaffold and tumor evolution. Curr. Opin. Cell Biol. 22: 697–706.

9. Ulrich, T.A., A. Jain, K. Tanner, J.L. MacKay, and S. Kumar. 2010. Probing cellular mechanobiology in three-dimensional culture with collagen-agarose matrices. Biomaterials. 31: 1875–1884.

10. Lee, G.Y.H., and C.T. Lim. 2007. Biomechanics approaches to studying human diseases. Trends Biotechnol. 25: 111–118.

11. Huang, H., R.D. Kamm, and R.T. Lee. 2004. Cell mechanics and mechanotransduction: pathways, probes, and physiology. Am. J. Physiol. Cell Physiol. 287: C1–C11.

12. Rodriguez, M.L., P.J. McGarry, and N.J. Sniadecki. 2013. Review on Cell Mechanics: Experimental and Modeling Approaches. Appl. Mech. Rev. 65: 060801.

13. Gossett, D.R., H.T.K. Tse, S.A. Lee, Y. Ying, A.G. Lindgren, O.O. Yang, J. Rao, A.T. Clark, and D. Di Carlo. 2012. Hydrodynamic stretching of single cells for large population mechanical phenotyping. Proc. Natl. Acad. Sci. U.S.A. 109: 7630–7635.

14. Tse, H.T.K., D.R. Gossett, Y.S. Moon, M. Masaeli, M. Sohsman, Y. Ying, K. Mislick, R.P. Adams, J. Rao, and D. Di Carlo. 2013. Quantitative Diagnosis of Malignant Pleural Effusions by Single-Cell Mechanophenotyping. Sci. Transl. Med. 5: 212ra163.

15. Dudani, J.S., D.R. Gossett, H.T.K. Tse, and D. Di Carlo. 2013. Pinched-flow hydrodynamic stretching of single-cells. Lab Chip. 13: 3728–3734.

16. Khan, Z.S., and S.A. Vanapalli. 2013. Probing the mechanical properties of brain cancer cells using a microfluidic cell squeezer device. Biomicrofluidics. 7: 011806.

17. Lange, J.R., J. Steinwachs, T. Kolb, L.A. Lautscham, I. Harder, G. Whyte, and Ben Fabry. 2015. Microconstriction Arrays for High-Throughput Quantitative Measurements of Cell Mechanical Properties. Biophys. J. 109: 26–34.

18. Otto, O., P. Rosendahl, A. Mietke, S. Golfier, C. Herold, D. Klaue, S. Girardo, S. Pagliara, A. Ekpenyong, A. Jacobi, M. Wobus, N.T.O. pfner, U.F. Keyser, J.O.R. Mansfeld, E. Fischer-Friedrich, and J. Guck. 2015. Real-time deformability cytometry: on-the-fly cell mechanical phenotyping. Nat. Methods. 12: 199–202.

19. Mietke, A., O. Otto, S. Girardo, P. Rosendahl, A. Taubenberger, S. Golfier, E. Ulbricht, S. Aland, J. Guck, and E. Fischer-Friedrich. 2015. Extracting Cell Stiffness from Real-Time Deformability Cytometry: Theory and Experiment. Biophys. J. 109: 2023–2036.

20. Lee, S.S., Y. Yim, K.H. Ahn, and S.J. Lee. 2009. Extensional flow-based assessment of red blood cell deformability using hyperbolic converging microchannel. Biomed.

Microdevices. 11: 1021–1027.

21. Yaginuma, T., M.S.N. Oliveira, R. Lima, T. Ishikawa, and T. Yamaguchi. 2013. Human red blood cell behavior under homogeneous extensional flow in a hyperbolic-shaped microchannel. Biomicrofluidics. 7: 054110.

22. Faustino, V., D. Pinho, T. Yaginuma, R.C. Calhelha, I.C.F.R. Ferreira, and R. Lima. 2014. Extensional flow-based microfluidic device: deformability assessment of red blood cells in contact with tumor cells. BioChip J. 8: 42–47.

23. Zeng, N.F., and W.D. Ristenpart. 2014. Mechanical response of red blood cells entering a constriction. Biomicrofluidics. 8: 064123.

24. Rodrigues, R.O., D. Pinho, V. Faustino, and R. Lima. 2015. A simple microfluidic device for the deformability assessment of blood cells in a continuous flow. Biomed. Microdevices. 17: 108.

25. Xia, Y., and G.M. Whitesides. 1998. Soft Lithography. Annu. Rev. Mater. Sci. 28: 153–184.

26. Deleyrolle, L.P., A. Harding, K. Cato, F.A. Siebzehnrubl, M. Rahman, H. Azari, S. Olson, B. Gabrielli, G. Osborne, A. Vescovi, and B.A. Reynolds. 2011. Evidence for label-retaining tumour-initiating cells in human glioblastoma. Brain. 134: 1331–1343.

27. Deleyrolle, L.P., and B.A. Reynolds. 2009. Identifying and enumerating neural stem cells: application to aging and cancer. Prog. Brain Res. 175: 43–51.

28. Taylor, G.I. 1934. The Formation of Emulsions in Definable Fields of Flow. pp. 501–523.

29. Karnis, A., and S.G. Mason. 1967. Particle motions in sheared suspensions: XXIII. Wall migration of fluid drops. J. Colloid Interface Sci. 24: 164–169.

30. Bentley, B.J., and L.G. Leal. 1986. An experimental investigation of drop deformation and breakup in steady, two-dimensional linear flows. J. Fluid Mech. 167: 241–283.

31. Milliken, W.J., and L.G. Leal. 1991. Deformation and breakup of viscoelastic drops in planar extensional flows. J. Non-Newtonian Fluid Mech. 40: 355–379.

32. Kon, K., N. Maeda, and T. Shiga. 1987. Erythrocyte deformation in shear flow: influences of internal viscosity, membrane stiffness, and hematocrit. Blood. 69: 727–734.

33. Guillou, L., A. Babataheri, P.-H. Puech, A.I. Barakat, and J. Husson. 2016. Dynamic monitoring of cell mechanical properties using profile microindentation. Sci. Rep. 6: 21529.

34. Hogan, B., A. Babataheri, Y. Hwang, A.I. Barakat, and J. Husson. 2015. Characterizing Cell Adhesion by Using Micropipette Aspiration. Biophys. J. 109: 209–219.

35. Haward, S.J., T.J. Ober, M.S.N. Oliveira, M.A. Alves, and G.H. McKinley. 2012. Extensional rheology and elastic instabilities of a wormlike micellar solution in a microfluidic cross-slot device. Soft Matter. 8: 536–555.

36. Stone, H.A. 2007. Introduction to Fluid Dynamics for Microfluidic Flows. In: Lee H, RM Westervelt, D Ham, editors. CMOS Biotechnology. Boston, MA: Springer US. pp. 5–30.

37. Kantsler, V., E. Segre, and V. Steinberg. 2008. Critical Dynamics of Vesicle Stretching Transition in Elongational Flow. Phys. Rev. Lett. 101: 048101.

38. Murata, T. 1981. Deformation of an elastic particle suspended in an arbitrary flow field. J. Phys. Soc. Jpn. 50: 1009–1016.

39. Fabry, B., G.N. Maksym, J.P. Butler, M. Glogauer, D. Navajas, and J.J. Fredberg. 2001. Scaling the Microrheology of Living Cells. Phys. Rev. Lett. 87: 148102.

40. Trepat, X., L. Deng, S.S. An, D. Navajas, D.J. Tschumperlin, W.T. Gerthoffer, J.P. Butler, and J.J. Fredberg. 2007. Universal physical responses to stretch in the living cell. Nature. 447: 592–595.

41. Alcaraz, J., L. Buscemi, M. Grabulosa, X. Trepat, B. Fabry, R. Farre, and D. Navajas. 2003. Microrheology of human lung epithelial cells measured by atomic force microscopy. Biophys. J. 84: 2071–2079.

42. Theret, D.P., M.J. Levesque, M. Sato, R.M. Nerem, and L.T. Wheeler. 1988. The Application of a Homogeneous Half-Space Model in the Analysis of Endothelial Cell Micropipette Measurements. J. Biomech. Eng. 110: 190–199.

43. Edmond, E., S. Farquhar, J.R. Dunstone, and A.G. Ogston. 1968. The osmotic behaviour of Sephadex and its effects on chromatography. Biochem. J. 108: 755–763.

44. Evans, I.D., and A. Lips. 1990. Concentration dependence of the linear elastic behaviour of model microgel dispersions. J. Chem. Soc., Faraday Trans. 86: 3413–3417.

45. Shin, J.H., M.L. Gardel, L. Mahadevan, P. Matsudaira, and D.A. Weitz. 2004. Relating microstructure to rheology of a bundled and cross-linked F-actin network in vitro. Proc. Natl. Acad. Sci. U.S.A. 101: 9636–9641.

46. Rotsch, C., K. Jacobson, and M. Radmacher. 1999. Dimensional and mechanical dynamics of active and stable edges in motile fibroblasts investigated by using atomicforce microscopy. Proc. Natl. Acad. Sci. U.S.A. 96: 921–926.

47. Solon, J., I. Levental, K. Sengupta, P.C. Georges, and P.A. Janmey. 2007. Fibroblast Adaptation and Stiffness Matching to Soft Elastic Substrates. Biophys. J. 93: 4453–4461.

48. Wottawah, F., S. Schinkinger, B. Lincoln, R. Ananthakrishnan, M. Romeyke, J. Guck, and J. Käs. 2005. Optical Rheology of Biological Cells. Phys. Rev. Lett. 94: 098103.

49. Chan, C.J., A.E. Ekpenyong, S. Golfier, W. Li, K.J. Chalut, O. Otto, J. Elgeti, J. Guck, and F. Lautenschlaeger. 2015. Myosin II Activity Softens Cells in Suspension. Biophys. J. 108: 1856–1869.

50. Zhou, E.H., S.T. Quek, and C.T. Lim. 2010. Power-law rheology analysis of cells undergoing micropipette aspiration. Biomech. Model. Mechanobiol. 9: 563–572.

51. Galli, R., E. Binda, U. Orfanelli, B. Cipelletti, A. Gritti, S. De Vitis, R. Fiocco, C. Foroni, F. Dimeco, and A. Vescovi. 2004. Isolation and Characterization of Tumorigenic, Stem-like Neural Precursors from Human Glioblastoma. Cancer Res. 64: 7011–7021.

52. Bao, S., Q. Wu, R.E. McLendon, Y. Hao, and Q. Shi. 2006. Glioma stem cells promote radioresistance by preferential activation of the DNA damage response. Nature. 444: 756–760.

53. Wong, S.Y., T.A. Ulrich, L.P. Deleyrolle, J.L. MacKay, J.M.G. Lin, R.T. Martuscello, M.A. Jundi, B.A. Reynolds, and S. Kumar. 2015. Constitutive Activation of Myosin-Dependent Contractility Sensitizes Glioma Tumor-Initiating Cells to Mechanical Inputs and Reduces Tissue Invasion. Cancer Res. 75: 1113–1122.

54. Guck, J., S. Schinkinger, B. Lincoln, F. Wottawah, S. Ebert, M. Romeyke, D. Lenz, H.M. Erickson, R. Ananthakrishnan, D. Mitchell, J. Käs, S. Ulvick, and C. Bilby. 2005. Optical Deformability as an Inherent Cell Marker for Testing Malignant Transformation and Metastatic Competence. Biophys. J. 88: 3689–3698.

55. Schmid-Schonbein, G.W., Y.Y. Shih, and S. Chien. 1980. Morphometry of human leukocytes. Blood. 56: 866–875.

56. Ronald, J.A., C.V. Ionescu, K.A. Rogers, and M. Sandig. 2001. Differential regulation of transendothelial migration of THP-1 cells by ICAM-1/LFA-1 and VCAM-1/VLA-4. J. Leukocyte Biol. 70: 601–609.

57. Ribeiro, C.M.P., J. Reece, and J.W. Putney. 1997. Role of the Cytoskeleton in Calcium Signaling in NIH 3T3 Cells. J. Biol. Chem. 272: 26555–26561.

58. Ailenberg, M., and M. Silverman. 2003. Cytochalasin D disruption of actin filaments in 3T3 cells produces an anti-apoptotic response by activating gelatinase A extracellularly and initiating intracellular survival signals. Biochim. Biophys. Acta, Mol. Cell Res. 1593: 249–258.

59. Moeendarbary, E., L. Valon, M. Fritzsche, A.R. Harris, D.A. Moulding, A.J. Thrasher, E. Stride, L. Mahadevan, and G.T. Charras. 2013. The cytoplasm of living cells behaves as a poroelastic material. Nat. Mater. 12: 253–261.

60. Zhao, H., and E.S.G. Shaqfeh. 2013. The shape stability of a lipid vesicle in a uniaxial extensional flow. J. Fluid Mech. 719: 345–361.

61. Narsimhan, V., A.P. Spann, and E.S.G. Shaqfeh. 2014. The mechanism of shape

instability for a vesicle in extensional flow. J. Fluid Mech. 750: 144–190.

62. Dahl, J.B., V. Narsimhan, B. Gouveia, S. Kumar, E.S.G. Shaqfeh, and S.J. Muller. 2016. Experimental observation of the asymmetric instability of intermediate-reduced-volume vesicles in extensional flow. Soft Matter. 12: 3787–3796.

63. Bevington, P.R., and D.K. Robinson. 2003. Data Reduction and Error Analysis for the Physical Sciences. Third. New York: McGraw-Hill.

SUPPORTING CITATIONS

Reference #63 appears in the Supporting Material.

Measuring cell viscoelastic properties using a microfluidic extensional flow device

L Guillou[†], JB Dahl[†], JM Lin[†], AI Barakat, J Husson, SJ Muller, S Kumar[*]

†These authors contributed equally to this work
*Corresponding author

SUPPORTING MATERIAL

SUPPORTING RESULTS

Derivation of the normalized entrance velocity ξ that best matches experimental measurements

Experimental values for ξ will lie between ξ_{min} and ξ_{max}, provided that we restrict our analysis to objects that are near the center of the channel. In such instances, the objects will be spread in the vertical axis between the heights r and h-r, where r is the radius of the spherical object. Indeed, it is not possible for a spherical object's center to get closer to the channel walls than r. We show an example in Figure 1B (dotted black line) where r = h/16, corresponding to an experimental case in which the channel height is 200 μm and the object's radius is at least 25 μm. To obtain those ξ values, we take the mean velocity along the heights considered using the velocity profile provided in Ref. (26). We find using these formulas that for our devices and objects (both dextran beads and cells), the analytical values for ξ are close to 1.5 (between 1.48 and 1.62). We also experimentally measure object velocities in the cross-slot, and find that they are about 1.5 times the mean velocity in the channel. Therefore, for simplicity, we use the value ξ = 1.5 in our experimental analysis.

Cells do not perturb the flow sufficiently to modify the strain rate in the device

For the calculations of strain rate in the cross-slot, it is assumed that the flow field is unaffected by suspended cells. To determine if the presence of cells in the fluid flow affects the fluid velocity and gradients, we inspect the Stokes number of the suspended cells, which is the ratio of particle momentum relaxation time (i.e. exponential decay of particle velocity due to drag) to the characteristic time scale of the continuum fluid phase. For neutrally buoyant particles with a small particle Reynolds number ($Re_p = Re(d_p^2/D^2) = \rho U d_p^2/(\mu D) < 0.013$), the momentum relaxation time scale is independent of density and can be expressed as $\tau_{mom} = d_p^2/(18\nu_c)$ where $\nu_c = \mu_c/\rho_c$ is the kinematic viscosity of the continuum fluid phase and d_p the diameter of the dispersed particles. Cells with a typical diameter of 10 μm and suspended in 20% w/v PEG20000/PBS ($\rho_c \sim 1040$ kg/m^3, $\mu_c \sim 0.04$ Pa·s) thus have a momentum relaxation time of $\tau_{mom} = 1.4 \cdot 10^{-7}$ seconds. The characteristic flow time scale is taken to be the inverse of the velocity gradient in the cross-slot region, **Ω**. The smallest strain rate in our cell cross-slot experiments is $\Omega = 34$ s^{-1}, leading to a maximum characteristic flow field time scale of $\tau_{flow} = 2.9 \cdot 10^{-2}$ seconds. Thus, the Stokes number for our cell cross-slot experiments $Stk = \tau_{mom}/\tau_{flow} = 5 \cdot 10^{-6} << 1$. Thus, the suspended cells follow the flow field streamlines instantaneously, and the strain rate in a cross-slot device **Ω** is undisturbed by the presence of the cells.

Uncertainty in cell strain measurements: User bias and small strains

We verified that the manual strain measurement was accurate within 2% strain by having different individuals analyze the same set of cells and set of cross-slot experiments (Supporting Figure S3). Observed cell strains were small at the lower strain rates, so that the difference in length of the major and minor axes was close to 1 pixel. We mitigated the limitation of resolving small deformations by measuring several cells per data point ($10 \leq n \leq 30$), which resulted in a clear trend of increasing strain with increasing strain rate for both cell types and all pharmacological conditions.

Viscous forces acting on a virtual spherical or ellipsoidal surface in planar extensional flow

The suspending fluid that is considered to be a Newtonian fluid has a Cauchy stress tensor of the form $\mathbf{T} = -\text{grad}(p) + \mu(\text{grad}(\mathbf{v}) + \text{grad}(\mathbf{v})^T)$ where p is the fluid pressure, μ the dynamic viscosity, and $\mathbf{v}$ the fluid velocity. Assume that the perturbations to the fluid velocity field due the presence of the cell are small, which is reasonable for our system as argued above. Due to the uniform velocity gradient in planar extensional flow $\text{grad}(\mathbf{v}) = [-\Omega\ 0\ 0;\ 0\ \Omega\ 0;\ 0\ 0\ 0]$ where Ω is the extensional strain rate, the viscous contribution to the fluid stress tensor is independent of location in the extensional flow field. Therefore, the force from the fluid (traction vector $\mathbf{t} = \mathbf{Tn}$) acting on the cell surface only depends on the local outward unit normal vector $\mathbf{n}$ of the cell surface. The viscous force vectors on the equator of a sphere and ellipsoid located anywhere in planar extensional flow, not just the stagnation point, are shown in Supporting Figure S7. The magnitude of each fluid force vector is proportional to $\mu\Omega$ and the z-component of the normal vector.

Micro Particle Image Velocimetry Measurements

We performed micro-PIV measurements using methods detailed in Ref. 62. Briefly, PIV measurements were performed in the cross-slot device used in most cell deformation experiments (w = 100 µm wide, h = 30 µm deep, and entrance channel length 1 mm) using a neutrally-buoyant suspension of ~0.1% v/v 1 mm fluorescent polystyrene spheres (FluoSpheres, ex/em 540/560 nm, Molecular Probes) in a 0.367 M sucrose solution (Sigma). We flow the suspension into the device gently by gravity because the syringe pump stepper motor is not fine enough to smoothly deliver flow at low enough velocities for accurate PIV measurements. Movies are captured with a CCD camera (Photometrics CoolSNAP HQ2) using NIS Elements software (Nikon) at a rate of 20 fps and an exposure time of 200 µs. PIV movies of the spheres were taken near the stagnation point using a 40x objective (3.03 pixel per µm at 2x2 binning, image size 696x520 pixels). Movies were taken using a Nikon TE2000-E2 microscope in fluorescent mode with the TRITC filter with a 40x objective (3.03 pixel per µm). The plane of focus was the device centerplane. For the PIV analysis, we sampled interrogation areas of 32x32 pixels with 50% overlap and use 250 frames in a typical movie.

Due to the gravity-driven flow being adjusted by hand, the stagnation point was slightly off-center from the device geometry. Horizontal displacement of the stagnation point with respect to the device center is due to two reservoirs supplying inlet flow on separate lab jacks being adjusted according to our visual check of stagnation point location. Slight differences in outlet tubing length or submersion depth in the outlet reservoir lead to the vertical displacement of the

stagnation point. The contour plot of velocity magnitude is not as smooth as our previous PIV measurements in the deeper cross-slot (383 μm deep in Ref. 62) used for vesicles because of a low particle concentration and the device thinness that leads to all particles in the channel (fast near the center and slow near the walls) being within the depth of focus. Due to the similar size of the device depth and microscope system field of depth, we can visualize all particles in the channel from those moving at the maximum fluid velocity at the centerplane and those closer to the walls moving at a slower velocity. Assuming the particles are evenly distributed across the device thickness, we conjecture that our PIV measurements are of the flow velocity averaged across the device thickness.

SUPPORTING FIGURES AND TABLES

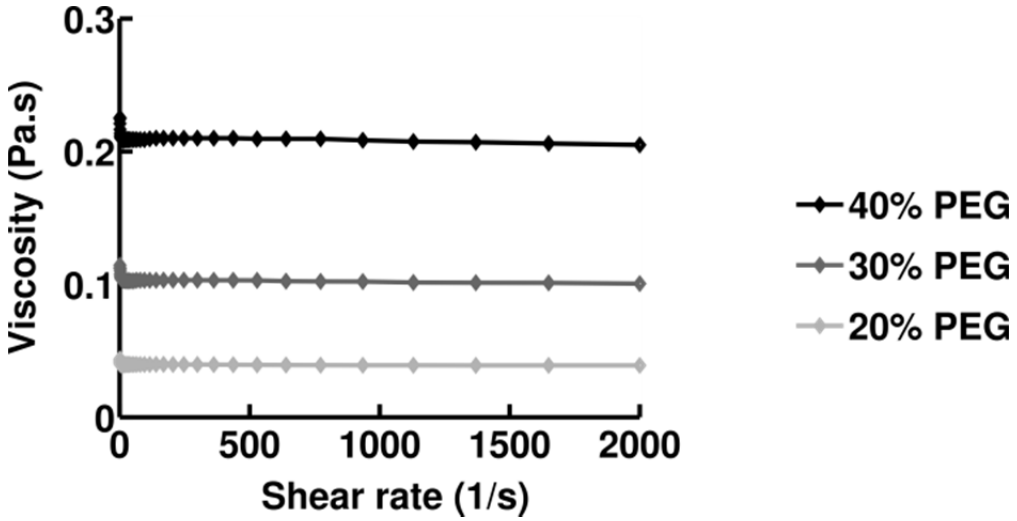

Supporting Figure S1. Macroscale rheologic measurements of PEG20000/PBS solutions used in cell cross-slot deformation experiments. Black line indicates 40% w/v PEG20000 in PBS, dark grey line indicates 30% w/v and light grey line 20% w/v. After initial transients at the experiment start-up, the viscosity is constant for strain rates of 1–2000 s^{-1} indicating the fluid is Newtonian. The reported viscosities for each batch are the average of 2 independent rheometry measurements.

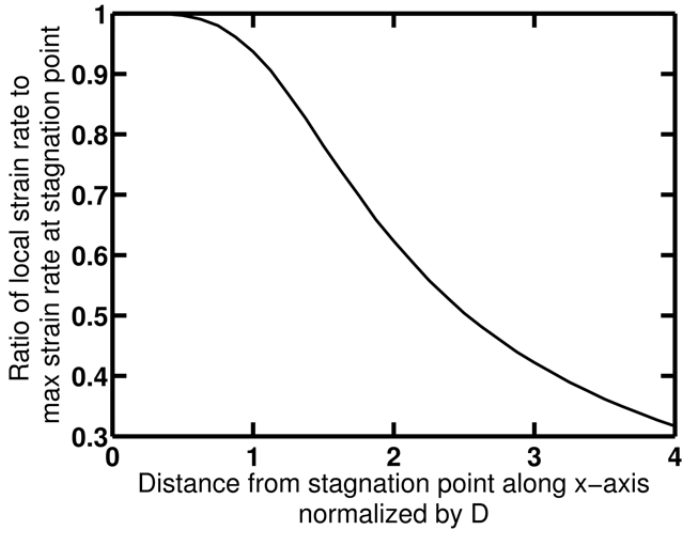

Supporting Figure S2. Ratio of local strain rate $\dot{\varepsilon}$ = du/dx to maximum strain rate at the cross-slot stagnation point as a function of the distance along the central inlet streamline as predicted in Hele-Shaw simulations. This streamline corresponds to the x-axis (cf. Figure 1A). The strain rate is approximately constant within a distance D (the channel half width) of the stagnation point, an indication that the flow field is indeed hyperbolic extensional flow. Thus, objects in the stagnation point region experience a constant strain rate.

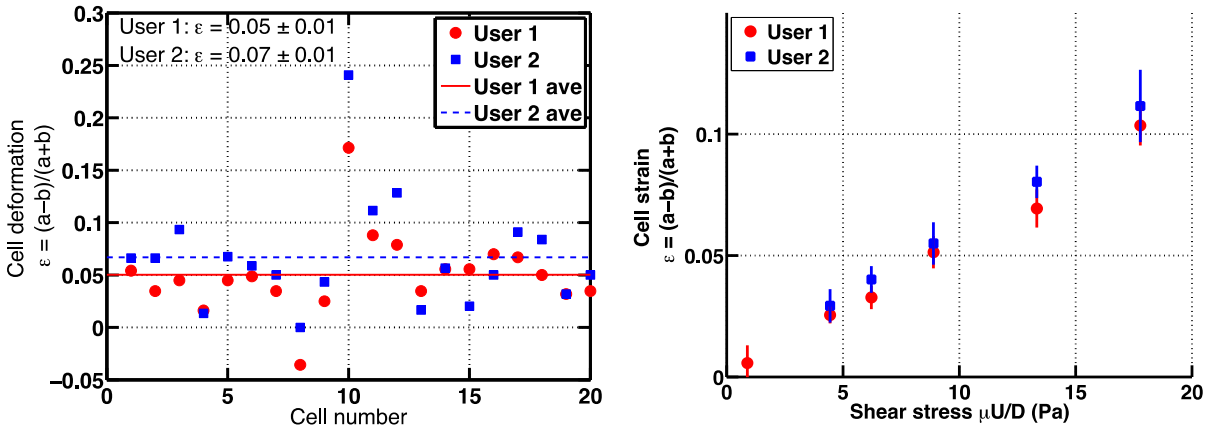

Supporting Figure S3. Impact of user bias on cell strain measurements is negligible. Left: Independent strain measurements performed by two users of a set of individual cells from a single cross-slot experiment (TIC control case, flow rate 300 μL/hr). Right: Independent cell strain measurements for several flow rates for control TICs by two users. Each marker is the average strain of n ≥ 10 cells and the error bars indicate ± standard error of the mean. Users independently selected qualifying cells to analyze and manually fitted ellipses in order to measure cell strain. User 2 systematically measures larger cell strain but agrees closely with User 1. For the results reported in the manuscript, User 1 performed most of the measurements.

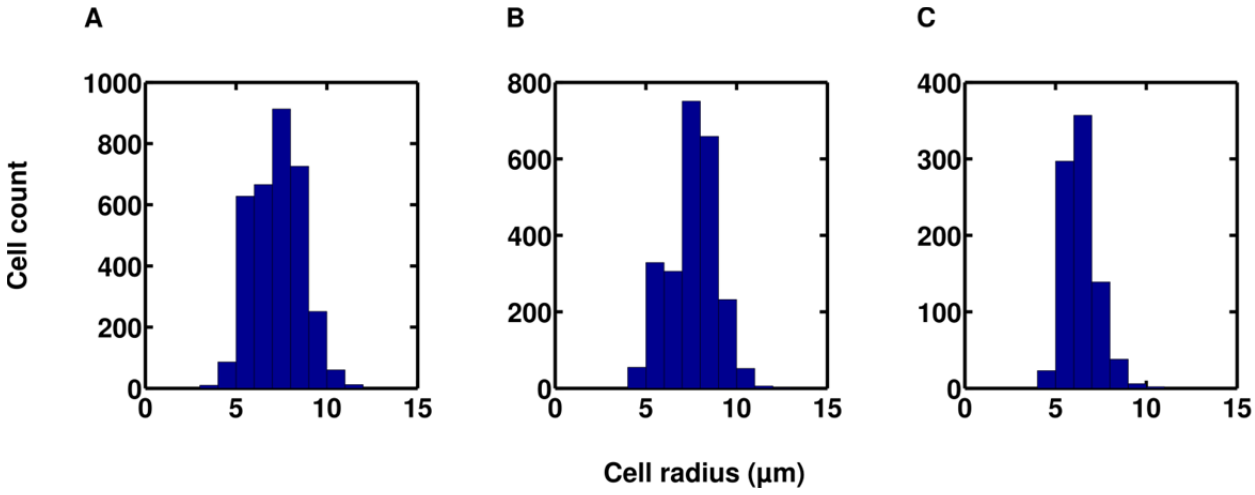

Supporting Figure S4. Histogram of cell radii. All analyzed cells are included. (A) Both TIC and 3T3 cells, in both control and drug conditions, are included (n = 3,357 cells). (B) Only TICs in control case are included (n = 1,288 cells). (C) Only 3T3 cells in control case are included (n = 321 cells).

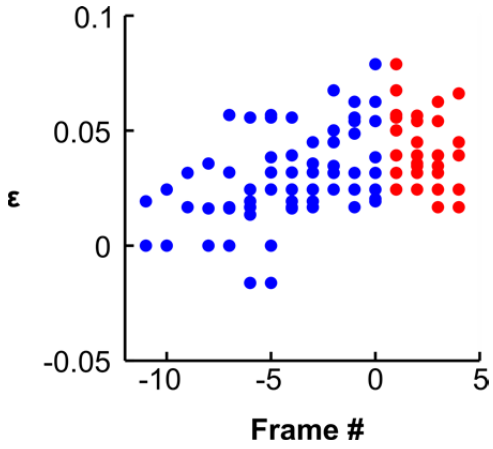

Supporting Figure S5. Cell deformation increases as they enter the cross-slot's central region $|\mathbf{x}| \leq D$ (blue dots), up until the point where they leave the central region and the deformation starts decreasing (red dots). Frame 0 marks the entry of the central region of the cross-slot. Cell deformation was tracked from the moment they entered the central region. Frame rate is approximately 40 fps. The cells in this example are 3T3 cells in control case at a flow rate of 250 µl/hr, with n = 8 cells tracked in this example.

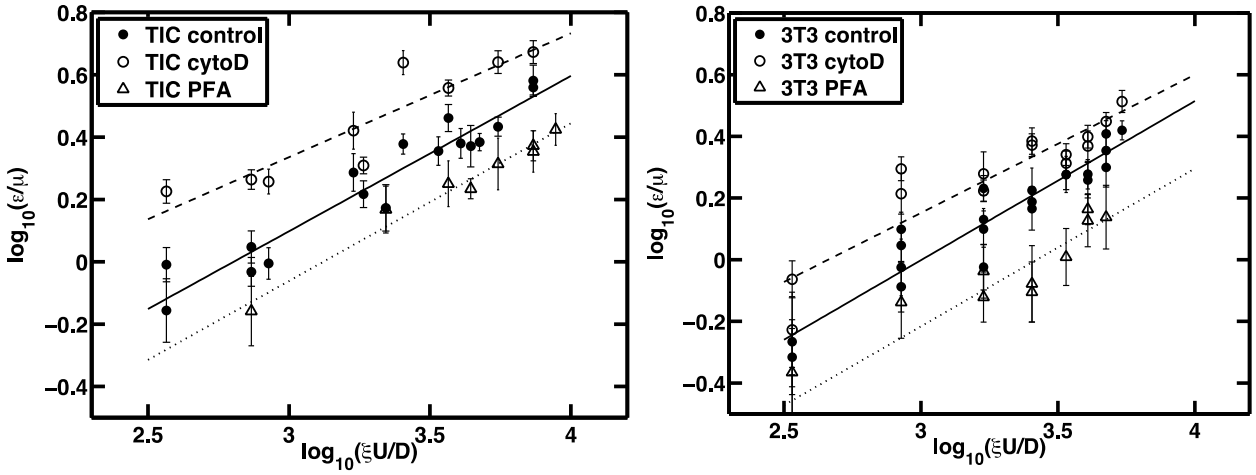

Supporting Figure S6. Cell cross-slot measurements including error bars reflecting the uncertainty in strain measurements (standard error of the mean). Error propagation (63) was used to plot these uncertainties for the quantity $\log(\varepsilon/\mu)$: $\sigma_{\log(\varepsilon/\mu)} = [d(\log(\varepsilon/\mu))/d\varepsilon]^2 \cdot (\sigma_\varepsilon)^2 = \sigma_\varepsilon/\varepsilon$.

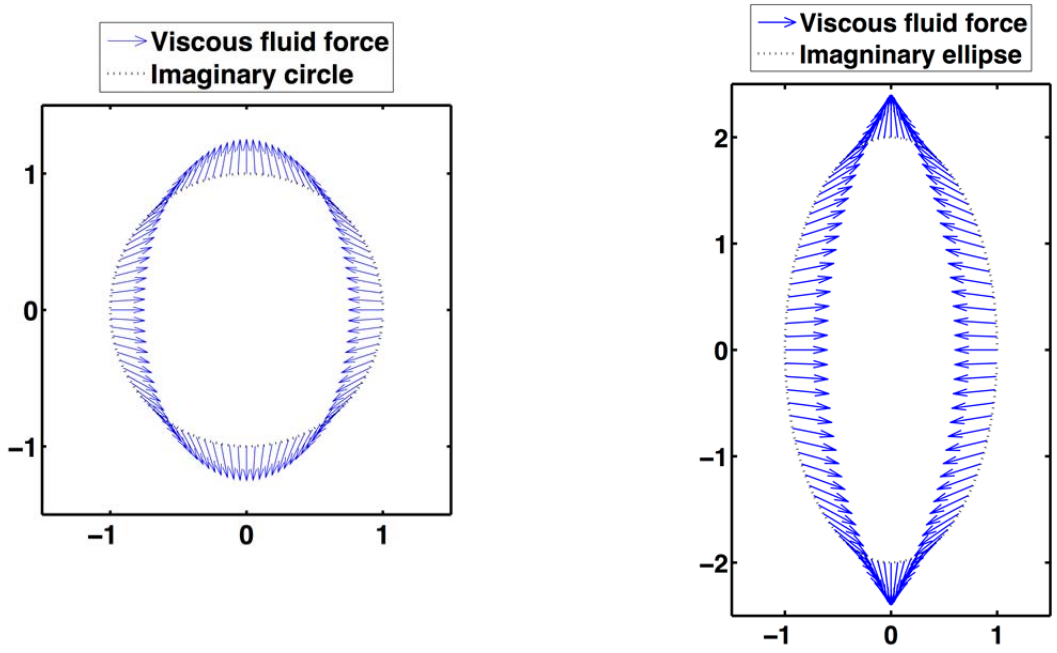

Supporting Figure S7. Viscous fluid forces acting on the surface of a sphere (left) and ellipsoid (right) in planar extensional flow that is unperturbed by the presence of the object. The force vectors in the x-y plane at the equator have a uniform magnitude equal to $2\mu\Omega$ (μ fluid viscosity, Ω extensional strain rate) and different directions.

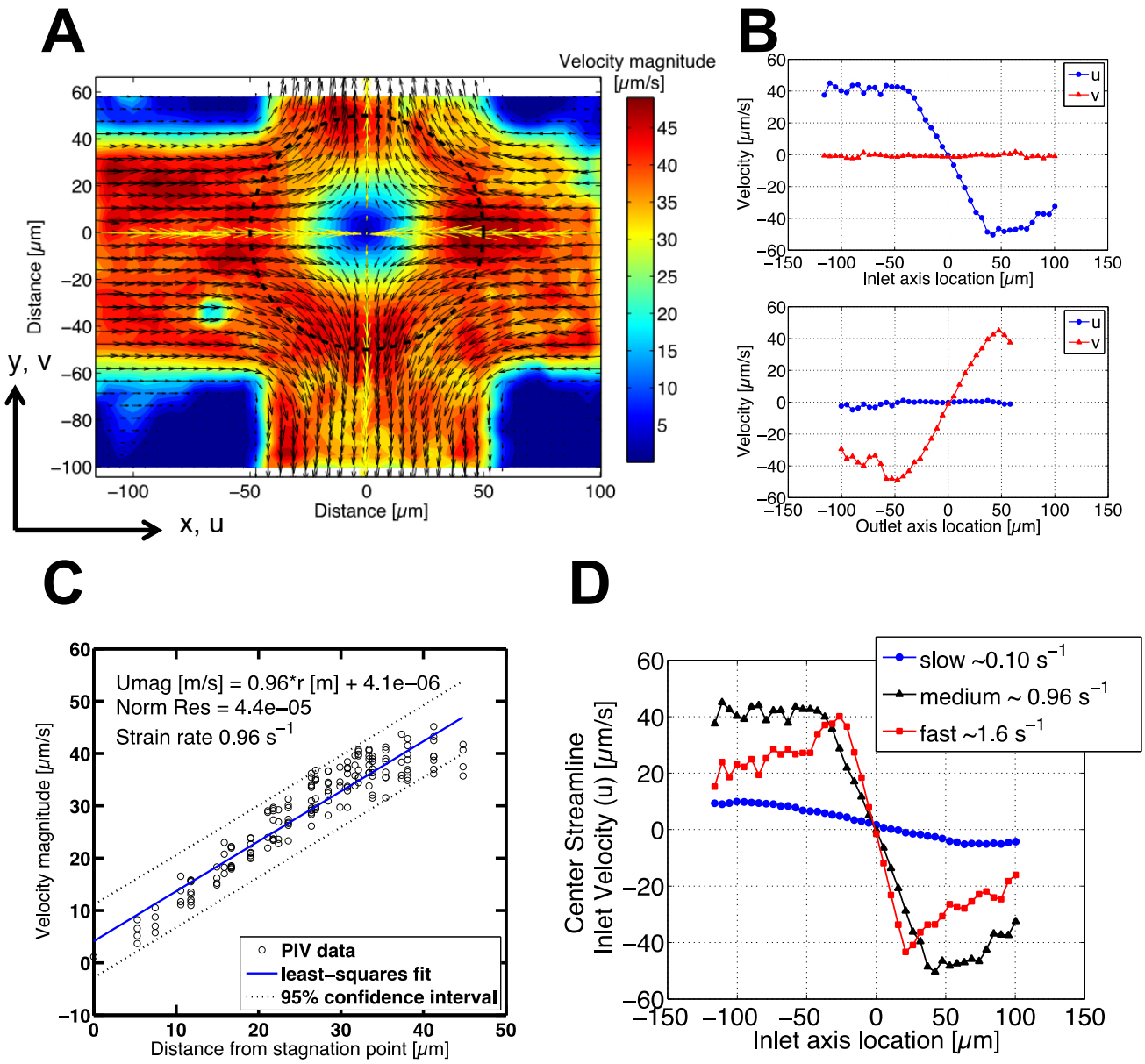

Supporting Figure S8. Micro Particle Image Velocimetry (PIV) measurements in cell cross-slot. Cross-slot dimensions are 100 μm wide (channel half-width D = 50 μm),height h = 30 μm, and entrance channel length of 1 mm. (A) Measured velocity vector field (arrows) and velocity magnitude (contour plot) indicated the presence of an extensional flow field. The black dashed line encloses the extensional flow stagnation point region ($|\mathbf{x}| = \mathrm{sqrt}(x^2 + y^2) \leq D$) in which the strain rate ($\dot{\varepsilon} = du/dx = -dv/dy \sim \xi U/D$) is constant. The stagnation point with zero velocity (u = v = 0) is located at (x,y) = (0,0). The yellow velocity vector arrows indicate the inlet and outlet centerline streamlines. Due to the gravity-driven flow being adjusted by hand, the stagnation point is slightly off-center from the cross-slot device. (B) The u and v components of velocity along the inlet (top) and outlet (bottom) streamlines for flow field plotted in (A). (C) The linear fit of the velocity magnitude as a function of distance to the stagnation point yields the measured extension rate near the stagnation point. The strongly linear behavior demonstrates that the flow within the stagnation region ($|\mathbf{x}| \leq D$) is indeed extensional flow. (D) Centerline inlet velocities (u component) for three different gravity-driven flow rates. The approximate strain rates as

measured by the linear fit method in (C) are indicated in the legend. Note that PIV velocity measurements are inaccurate for velocities above ~40 μm/s due to the particles traveling too fast relative to interrogation area size and time between frames. Thus the inlet velocities for the fast flow rate are aphysical for distances greater than 50 μm from the stagnation point. For the medium and slow flow rates, the centerline velocity decreases linearly from the entrance velocity to zero over a distance D = 50 μm.

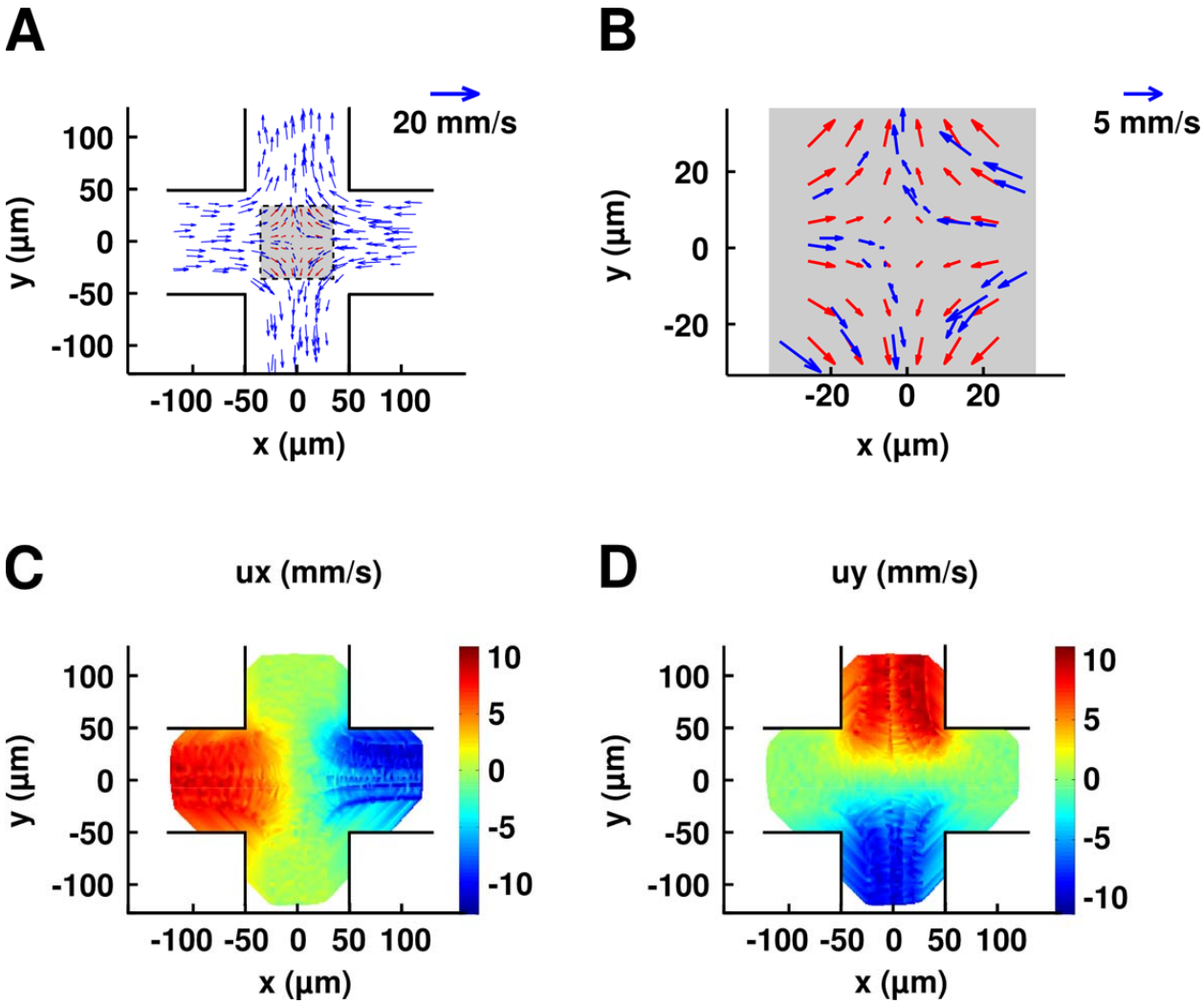

Supporting Figure S9. Cell flow pattern in cross-slot matches surrounding fluid flow pattern. (A) Plot of cell velocity vectors (blue arrows) overlaid at the center of the cross-slot with analytical values for fluid velocity (red arrows). x and y axis indicate the position. The experiment was done in a cross-slot of 100 µm width and 30 µm height, at a flow rate of 50 µL/hr. Blue arrow at the top right indicates velocity scale. Cells are 3T3 mouse fibroblasts. Cells were manually tracked using the MTrackJ plug-in in ImageJ. n = 38 cells were tracked and N = 2039 velocity measurements were performed (only 1 in 10 measurements are shown on in panel A for clarity). The square grey zone at the center corresponds to the zoom shown in panel B. (B) Zoom on the central region highlighted in grey in panel A. Same notations and conventions as in panel A apply. (C) Cell velocity ux along the x axis. ux was interpolated from N = 2039 velocity measurements performed under the same condition (see panel A for details). Under those conditions, U = 4.6 mm/s (mean fluid velocity) and $U_{max} \sim 1.5$ U = 6.9 mm/s. (D) Cell velocity uy along the y axis. Same notations and conventions as in panel C apply.

Supporting Table S1. Range for various experimental parameters over all experimental conditions tested for the glioblastoma tumor initiating cells (TIC) and 3T3 fibroblast cells. $U = Q/(h \cdot w)$ is the average flow velocity in the channels based on the specified flow rate Q and channel cross-sectional dimensions (width $w = 2 \cdot D$, height $h = 30$ μm). The suspending fluid viscosity μ was measured before each set of experiments (sample measurements Supporting Figure S1). The flow Reynolds number Re is based on microchannel dimensions, fluid properties, and flow rate. n is the number of cells used to determine the average strain ε that makes up each data point in Figure 4(B,C).

Cell Type	**μ**	**w**	**U**	**$Re = \rho UD/\mu$**	**$\xi U/D$**	**n**	**$\varepsilon = (a-b)/(a+b)$**
	[mPa·s]	[μm]	[mm/s]		s^{-1}		
TIC	$36 \le \mu \le 42$	$w = 70, 100$	$7 \le U \le 159$	$0.0057 \le Re \le 0.19$	$283 \le \xi U/D \le 6800$	$10 \le n \le 27$	$0.029 \le \varepsilon \le 0.18$
3T3	$37.5 \le \mu \le 38.3$	$w = 100$	$9 \le U \le 148$	$0.013 \le Re \le 0.20$	$278 \le \xi U/D \le 4440$	$10 \le n \le 30$	$0.009 \le \varepsilon \le 0.12$

Supporting Table S2. Statistical significance (p-values) of multiple regression analysis of covariance.

Comparison Groups	3T3 p-value	TIC p-value
Control vs. CytoD	0.012	0.0002
Control vs. PFA	0.0094	0.0015
CytoD vs. PFA	0.0004	$8.5 \cdot 10^{-6}$

Supporting Table S3. Raw data for glioblastoma tumor initiating cells (TIC) mechanical measurements. The uncertainty (σ_ε) in the average strain measurement (ε) at each experimental condition is the standard error of the mean.

TIC	Fluid viscosity μ	Channel wideth w = 2·D	Mean flow velocity U	Flow Reynolds number Re = ρUD/μ	Extensional strain rate ξU/D	Number of cells n	Average strain ε = (a-b)/(a+b)	Strain uncertainty σ_ε
	mPa·s	μm	mm/s		s^{-1}			std error of mean
TIC CONTROL								
Day 1	42	70	6.61	0.0057	283	14	0.029	0.007
			13.23	0.0115	567	15	0.047	0.006
			39.68	0.0344	1701	12	0.06	0.01
			79.37	0.0688	3401	16	0.10	0.02
			132.28	0.1146	5669	15	0.16	0.02
Day 2	36	100	23.15	0.0334	694	11	0.036	0.004
			46.30	0.0669	1389	15	0.07	0.01
			69.44	0.1003	2083	15	0.086	0.006
			92.59	0.1337	2778	15	0.082	0.009
			111.11	0.1605	3333	14	0.09	0.01
			129.63	0.1872	3889	11	0.087	0.006
Day 3	37.6	70	6.61	0.0064	283	12	0.037	0.005
			13.23	0.0128	567	18	0.035	0.004
			33.07	0.0320	1417	20	0.062	0.006
			66.14	0.0640	2834	20	0.11	0.01
			99.21	0.0960	4252	27	0.102	0.007
			132.28	0.1281	5669	22	0.136	0.008
TIC CYTOCHALASIN D								
Day 2	36	100	23.15	0.0334	694	18	0.065	0.006
			46.30	0.0669	1389	20	0.09	0.01
			69.44	0.1003	2083	15	0.16	0.01
Day 3	37.6	70	6.61	0.0064	283	14	0.063	0.005
			13.23	0.0128	567	16	0.069	0.005
			33.07	0.0320	1417	20	0.077	0.005
			66.14	0.0640	2834	20	0.136	0.008
			99.21	0.0960	4252	20	0.16	0.01
			132.28	0.1281	5669	20	0.18	0.02
TIC PFA								
Day 1	42	70	13.23	0.0115	567	20	0.029	0.007
			39.68	0.0344	1701	19	0.06	0.01
			79.37	0.0688	3401	18	0.072	0.005
			132.28	0.1146	5669	10	0.10	0.01
Day 3	37.6	70	66.14	0.0640	2834	20	0.07	0.01
			99.21	0.0960	4252	20	0.08	0.01
			132.28	0.1281	5669	20	0.08	0.01
			158.73	0.1537	6803	20	0.10	0.01

Supporting Table S4. Raw data for 3T3 fibroblast cell mechanical measurements. The uncertainty (σ_ε) in the average strain measurement (ε) at each experimental condition is the standard error of the mean.

3T3	Fluid viscosity μ	Channel wideth w = 2·D	Mean flow velocity U	Flow Reynolds number Re = ρUD/μ	Extensional strain rate ξU/D	Number of cells n	Average strain ε = (a-b)/(a+b)	Strain uncertainty σ_ε
	mPa·s	μm	mm/s		s^{-1}			std error of mean
3T3 CONTROL								
Day 1	37.75	100	23.15	0.0319	694	16	0.047	0.006
			46.30	0.0638	1389	11	0.047	0.006
			69.44	0.0957	2083	22	0.058	0.003
			111.11	0.1531	3333	15	0.071	0.008
			129.63	0.1786	3889	25	0.10	0.01
			148.15	0.2041	4444	27	0.099	0.007
Day 2	38.3	100	23.15	0.0314	694	10	0.043	0.005
			46.30	0.0629	1389	10	0.065	0.006
			69.44	0.0943	2083	11	0.056	0.009
			92.59	0.1257	2778	10	0.072	0.008
			111.11	0.1509	3333	10	0.069	0.009
			129.63	0.1760	3889	19	0.09	0.01
Day 3	37.5	100	23.15	0.0321	694	10	0.035	0.007
			46.30	0.0642	1389	10	0.051	0.004
			69.44	0.0963	2083	14	0.06	0.01
			92.59	0.1284	2778	13	0.07	0.01
Day 4	37.5	100	9.26	0.0128	278	10	0.020	0.007
			23.15	0.0321	694	18	0.031	0.006
			46.30	0.0642	1389	10	0.035	0.006
			129.63	0.1798	3889	12	0.07	0.01
3T3 CYTO D								
Day 1	37.75	100	9.26	0.0128	278	21	0.033	0.005
			23.15	0.0319	694	15	0.074	0.007
			46.30	0.0638	1389	30	0.063	0.005
			69.44	0.0957	2083	12	0.089	0.008
			92.59	0.1275	2778	10	0.083	0.007
			111.11	0.1531	3333	27	0.095	0.008
			129.63	0.1786	3889	10	0.106	0.007
			148.15	0.2041	4444	20	0.12	0.01
Day 2	38.3	100	9.26	0.0126	278	17	0.023	0.006
			23.15	0.0314	694	16	0.06	0.01
			46.30	0.0629	1389	12	0.07	0.01
			69.44	0.0943	2083	20	0.093	0.009
			92.59	0.1257	2778	21	0.079	0.007
			111.11	0.1509	3333	26	0.09	0.01
3T3 PFA								
Day 3	37.5	100	9.26	0.0128	278	15	0.016	0.005
			46.30	0.0642	1389	15	0.028	0.005
			69.44	0.0963	2083	15	0.031	0.009
			111.11	0.1541	3333	15	0.055	0.006
Day 4	37.5	100	9.26	0.0128	278	11	0.009	0.005
			23.15	0.0321	694	15	0.027	0.007
			46.30	0.0642	1389	15	0.034	0.007
			69.44	0.0963	2083	15	0.029	0.007
			92.59	0.1284	2778	14	0.038	0.008
			111.11	0.1541	3333	15	0.05	0.01
			129.63	0.1798	3889	15	0.05	0.01